Inorganic Chemistry

pubs.acs.org/IC Article

Putative O−O Bond Formation in the Coordination Sphere of a Bispidine-Iron(IV)-Oxido Complex

Katharina Bleher,[#] Thakur Rochak Kumar Rana,[#] Thomas Josephy, Fridolin Röhs, Thorsten Glaser, Hubert Wadepohl, Gopalan Rajaraman, and Peter Comba*

Cite This: *Inorg. Chem.* 2025, 64, 17672−17686 Read Online

ACCESS | Metrics & More | Article Recommendations | Supporting Information

Downloaded via INDIAN INST OF TECH BOMBAY on December 27, 2025 at 07:39:34 (UTC).
See https://pubs.acs.org/sharingguidelines for options on how to legitimately share published articles.

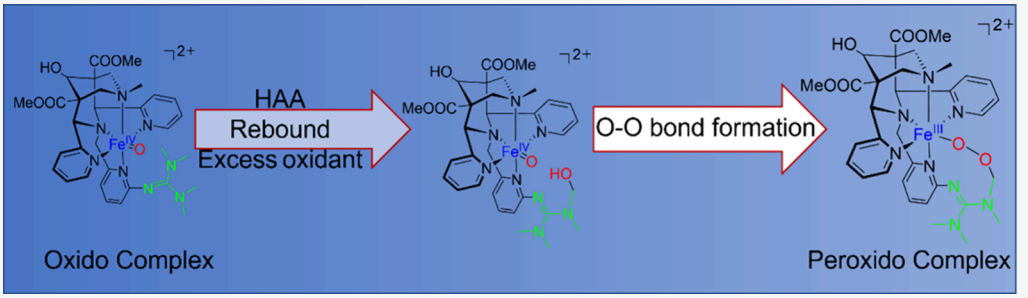

ABSTRACT: We present a pentadentate bispidine iron complex with a guanidine pendant group at one of the pyridine donors (bispidine = 3,7-diazabicyclo[3.3.1]nonane), whose iron(II) precursor can be oxidized with iodosylbenzene in strictly water- and oxygen-free solution to an iron(III) species that is a competent catalyst for oxygen atom transfer (OAT) to thioanisole. Time-dependent UV−vis−NIR spectroscopy and ESI and tandem mass spectrometry, supported by EPR and Mössbauer spectroscopy and the investigation of the OAT activity, lead to the conclusion that the active species is an iron(III)-peroxido complex and that its formation is initiated by an intramolecular C−H abstraction (HAA) at the guanidinyl substituent, followed by OH rebound to produce an iron(II) intermediate with a hydroxylated guanidinyl substituent. This is reoxidized to the corresponding iron(IV)-oxido intermediate, where the Fe^{IV}=O and ligand−OH groups are well preorganized for an intramolecular O−O bond formation. An outer-sphere oxidation then produces the iron(III)-peroxido complex, which relatively efficiently sulfoxidizes thioanisole. A detailed DFT-based computational study supports the experimental observations and indicates that the initial HAA is rate determining; that is, O−O bond formation is a very efficient process. The effectiveness of the initial HAA, that of the OH rebound and specifically that of the O−O bond formation, are shown to be due to the well preorganized coordination sphere of the iron-bispidine active species.

INTRODUCTION

Water is oxidized to molecular dioxygen in the natural photosynthetic cycle, and the released electrons are transported along the Z-scheme to reduce CO_2 to carbon-based feedstock in the dark reaction.[1−3] Transformation of solar to chemical energy with water as the substrate generally involves O−O bond formation, and the evolving protons and electrons often are used to produce hydrogen as a fuel,[4,5] but hydrogen peroxide[6] and other chemicals have also been considered.[7−9] In the oxygen evolving reaction, nature uses a high-valent manganese-oxido catalyst for the demanding O−O bond formation. Small molecule nonheme manganese and iron compounds have been used extensively for mechanistic work and to develop potentially useful catalysts.[10−16]

The rich chemistry of dioxygen activation and formation and the reactivity of high-valent metal−oxygen species (superoxido, peroxido, oxido, and the corresponding protonated or alkylated derivatives) have a long tradition in iron-based chemistry, and the thorough characterization of Fe^{IV}=O based enzymes and the development of model systems have led to a good understanding of the reactivities of the corresponding oxidants and the mechanistic landscape.[17−20] In our efforts to contribute to the understanding of nonheme iron reactivities, we have concentrated on ligands based on the bispidine scaffold (bispidine = 3,7-diazabicyclo[3.3.1]nonane, see Scheme 1 for L^1 used in this study and relevant derivatives).[21−24] The main feature of bispidine-ferryl oxidants is the rigid and relatively large ligand cavity,[25−28] enforcing high redox potentials as well as small in-plane ligand fields and hence small triplet-quintet gaps in the S = 1 Fe^{IV}=O species.[29−31] Indeed, to date, one of our (bispidine)Fe^{IV}=O

Received: March 26, 2025
Revised: August 12, 2025
Accepted: August 14, 2025
Published: August 27, 2025

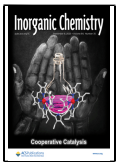

ACS Publications © 2025 American Chemical Society

Scheme 1. Ligand L^1 Used in This Study with Atom Numbering and Synthetic Pathway Starting from the Known L^2 and Other Bispidine Derivatives Mentioned in the Text

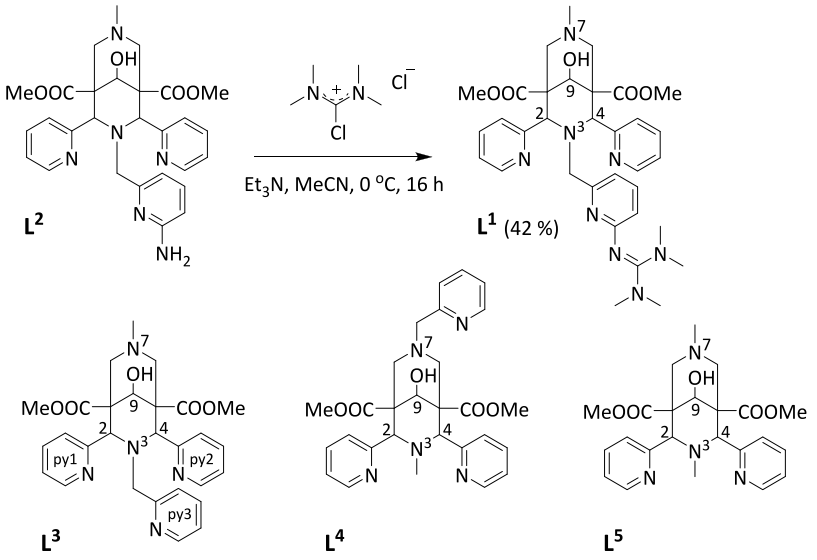

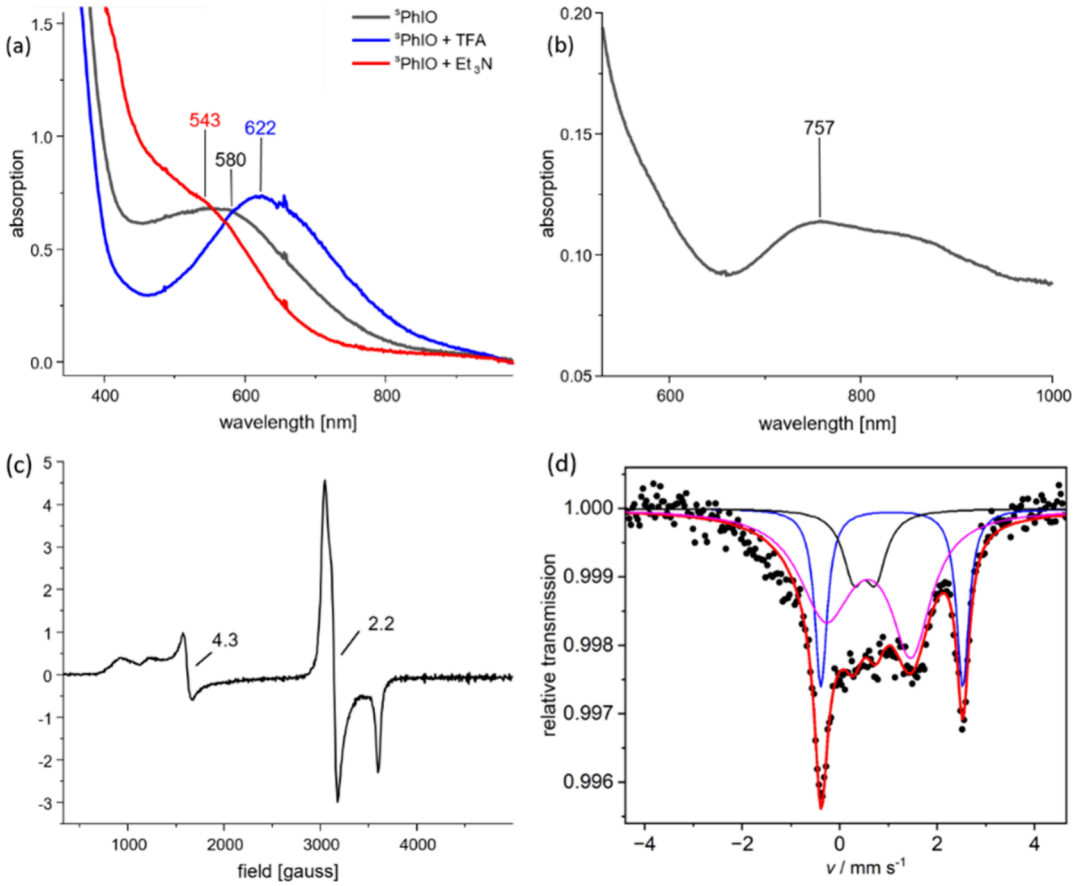

Figure 1. (a) UV−vis−NIR spectra of $[(L^1)Fe^{II}(NCMe)]^{2+}$ (0.5 mM) with 6 eq of ^{s}PhIO at rt in MeCN. To this solution, either 5 eq of TFA (protonation of the Fe^{III}-peroxido species) or Et_3N (deprotonation of the Fe^{III}-hydroperoxido species) were added; these processes are reversible, but the deprotonated species slowly decays in rt solutions. (b) UV−vis−NIR spectra of $[(L^1)Fe^{II}(NCMe)]^{2+}$ (0.5 mM) with 0.8 eq of ^{s}PhIO at −20 °C in MeCN, producing $[(L^1)Fe^{IV}{=}O]^{2+}$. (c) EPR spectrum of the Fe^{III}-peroxido species (9.632103 GHz, 8.3 K, 2 mM Fe^{II} in MeCN, and excess ^{s}PhIO). (d) Mössbauer spectrum of 1 mM $[(L^1)^{57}Fe^{II}(NCMe)]^{2+}$ in MeCN, with 0.9 eq of ^{s}PhIO, added at 0 °C and frozen as quickly as possible, resulting in the Fe^{II} precursor (blue), a low-spin Fe^{III} species (magenta), and a high-spin Fe^{III} species (black).

complexes is the most efficient small molecule Fe^{IV}=O oxidant with a reactivity close to that of enzymes.[31−35]

Ligand substituents may help to shape the active site, stabilize intermediates, and activate substrates by secondary interactions, and substituents that have been used to shape the

https://doi.org/10.1021/acs.inorgchem.5c01373
Inorg. Chem. 2025, 64, 17672−17686

Table 1. Spectroscopic Properties of the $[(L)Fe^{III}–OOR]^{n+}$ (Peroxido, Hydroperoxido, Alkylperoxido) and $[(L)Fe^{IV}=O]^{n+}$ Complexes with the Guanidine Derived Ligand L^1[a]

parameter	$[(L^1)Fe^n(X)]^{m+}$	$[(L^3)Fe^n(X)]^{m+}$	$[(L^4)Fe^n(X)]^{m+c}$	$[(L^5)Fe^n(NCMe)(X)]^{m+}$
λ_{max} (Fe^{III}-η^1-OOH) [nm]	622 (630)	561[c21]	561[21]	605[cd44]
λ_{max} (Fe^{III}-η^2-OO) [nm]	543 (550)	780[b21]	721[b21]	
λ_{max} (Fe^{IV}=O) [nm]	757 (755)	730[45]	730[45]	755[46]
g (x,y,z) (Fe^{III}-η^1-OOR) R = alk, H[e]	2.18, 2.13, 1.92	2.18, 2.12, 1.95[c45]	2.19, 2.13, 1.96[45]	2.16, 2.13, 1.97[cd44]
δ, $\lvert\Delta E_Q\rvert$ (Fe^{II} prec) [mm s^{-1}]	1.07, 2.90 (1.11, 2.64)			1.14, 2.89[47]
δ, $\lvert\Delta E_Q\rvert$ (Fe^{III}–OOR) [mm s^{-1}]	0.59, 1.75 (0.69, 1.32)			
δ, $\lvert\Delta E_Q\rvert$ (Fe^{III}–OOH) [mm s^{-1}]	0.51, 0.45 (0.69, 0.58)			
δ, $\lvert\Delta E_Q\rvert$ (Fe^{IV}=O) [mm s^{-1}]		0.02, 0.69[c44]	0.01, 1.34[48]	0.07, 0.66[c47]

[a]DFT computed values in parentheses. Derivative L3 is unsubstituted pyridine at py3. Ligand L4 is an isomer of L3. L5 is a tetradentate bispidine. [b]Side-on peroxide. [c]Ketone at C9. [d](-OO^{t}Bu). [e]Fe^{III} part of the spectra.

active site in metal–oxygen species include amides and guanidines, and both have been used in the area of nonheme iron oxidants.[36−41] However, hydrogen bond donors close to the oxido group also bear the danger of undesired side reactions—an aspect that often (as in the present case) is not considered in the design process.

Here, we present the results of experiments with a guanidine-substituted pentadentate bispidine. Upon oxidation of the iron(II) precursor $[(L^1)Fe^{II}(NCMe)]^{2+}$ with iodosylbenzene, depending on the reaction conditions but in strictly water- and oxygen-free media, it is possible to trap and characterize the desired high-valent $[(L^1)Fe^{IV}=O]^{2+}$ oxidant and an iron(III) decay product, which in the reaction with thioanisole is shown to be a competent oxidant (OAT). The combination of mass spectrometry with the spectroscopic analysis of trapped intermediates, computational spectroscopy, and a detailed mechanistic study indicates that the sequence of reactions is initiated by an intramolecular C–H activation (HAA) that promotes a unique O–O bond formation, leading to an Fe^{III}-alkylperoxido complex with unusually high reactivity. An extensive quantum chemical analysis based on DFT calculations supports the proposed mechanistic pathway derived from experiment, provides insight into the efficiency and selectivity of the observed processes, and also rationalizes the rapid O–O bond formation and the reactivity of the peroxide product. The initiating HAA is, as expected from the C–H activation reactivity of similar iron-bispidine catalysts, an efficient reaction but is rate limiting, and this follows from the observed kinetics and is supported by the DFT-based analysis. The efficiency of the HAA, of the OH rebound step and, specifically, of the O–O bond formation is shown to be the result of the geometry of the iron-bispidine reactive site, a result of the preorganization of the rigid bispidine scaffold.

RESULTS AND DISCUSSION

Oxidation of the Fe^{II} Precursor. The guanidine-appended ligand L^1 was obtained in a simple one-step reaction involving alkylation of the previously described amine precursor L^2 (see Scheme 1).[42] Single crystals of the ligand for X-ray crystallographic analysis were obtained by recrystallization from ethyl acetate and were subsequently analyzed. The $[(L^1)Fe^{II}(NCMe)]^{2+}$ precursor was isolated as a yellow triflate salt. The preparation and characterization of the ligand and the Fe^{II} precursor are described in more detail in the Supporting Information, which also includes X-ray structural data of L^1 and $[(L^1)Fe^{II}(OH_2)](OTf)_2$ (Figure S1). In situ reaction of $[(L^1)Fe^{II}(NCMe)]^{2+}$ with excess iodosylbenzene (2–4 eq of the more soluble ^{t}Bu-sulfonyl derivative ^{s}PhIO; millimolar concentration of the Fe^{II} precursor in MeCN, rt, Ar) leads to a purple species ($\lambda_{max} \approx 580$ nm), reminiscent of an Fe^{III}-peroxido compound,[21−24] see Figure 1a (a similar electronic spectrum is observed when *tert*-butylperoxide (^{t}BuOOH) is used as the oxidant, Figure S6). With a substoichiometric amount of ^{s}PhIO at low temperature (0.8 eq, −20 °C), a metastable intermediate with typical d–d transitions for $S = 1$ Fe^{IV}=O ($\lambda_{max} = 757$ nm) is observed (Figure 1b), which quickly decays with the formation of a transition at ≈580 nm (Figure S3). The putative L^1 based Fe^{IV}=O complex is also observed when H_2O_2 is used as an oxidant (Figure S5).

The optical spectra of the major species with high intensity transitions around 540–625 nm are reminiscent of Fe^{III}-hydroperoxido/alkylperoxido/peroxido complexes with charge transfer transitions around 600 nm (spectroscopic data of the Fe^{III} and Fe^{IV}=O complexes are assembled and compared with published data of similar bispidine complexes in Table 1).[21,43−46] The EPR spectrum in Figure 1c, obtained from freezing a solution with an electronic transition around 580 nm (Figure 1a), has typical features of high-spin ($g \approx 4.3$) and low-spin Fe^{III} complexes ($g \approx 2.2$). The UV–vis–NIR and EPR spectra of solutions prepared as above and treated with acid or base (TFA, Et_3N) show that there is an equilibrium between a protonated and a deprotonated form of the Fe^{III}-peroxido species, where the protonated form has a low-spin electronic configuration with a CT transition at 622 nm, while the deprotonated form shows a higher ratio of the high-spin species and a CT transition at ≈543 nm (Figure 1, Table 1, Figure S7). These variations are akin to known spin-crossover bispidine-Fe^{III}-peroxido systems (Table 1; the spin-crossover equilibrium has been studied in detail for $[(L^4)$-$Fe^{III}OO^tBu]^{2+}$).[44]

The Mössbauer spectra from the reaction of $[(L^1)$-$Fe^{II}(NCMe)]^{2+}$ with ^{s}PhIO at 0 °C, followed by freezing with liquid N_2, vary depending on the amount of ^{s}PhIO added and time passed before freezing. Figure 1d shows a typical spectrum with some of the high-spin Fe^{II} precursor (see Figure S8 for the spectrum of the precursor) and at least two other species. Simulations with three species indicate the presence of two Fe^{III} compounds—one with a small quadrupole splitting (≈0.5 mm s^{-1}), typical for high-spin Fe^{III}, and one with a large quadrupole splitting (≈1.8 mm s^{-1}), typical for low-spin Fe^{III}. The latter was also obtained as a major species in one of the measurements (Figure S9) and provides a very broad and asymmetric quadrupole doublet with $\delta = 0.59$ mm s^{-1} and $\lvert\Delta E_Q\rvert = 1.75$ mm s^{-1}. Using these values and those of the high-spin Fe^{II} precursor provides a consistent fit with three

https://doi.org/10.1021/acs.inorgchem.5c01373
Inorg. Chem. 2025, 64, 17672−17686

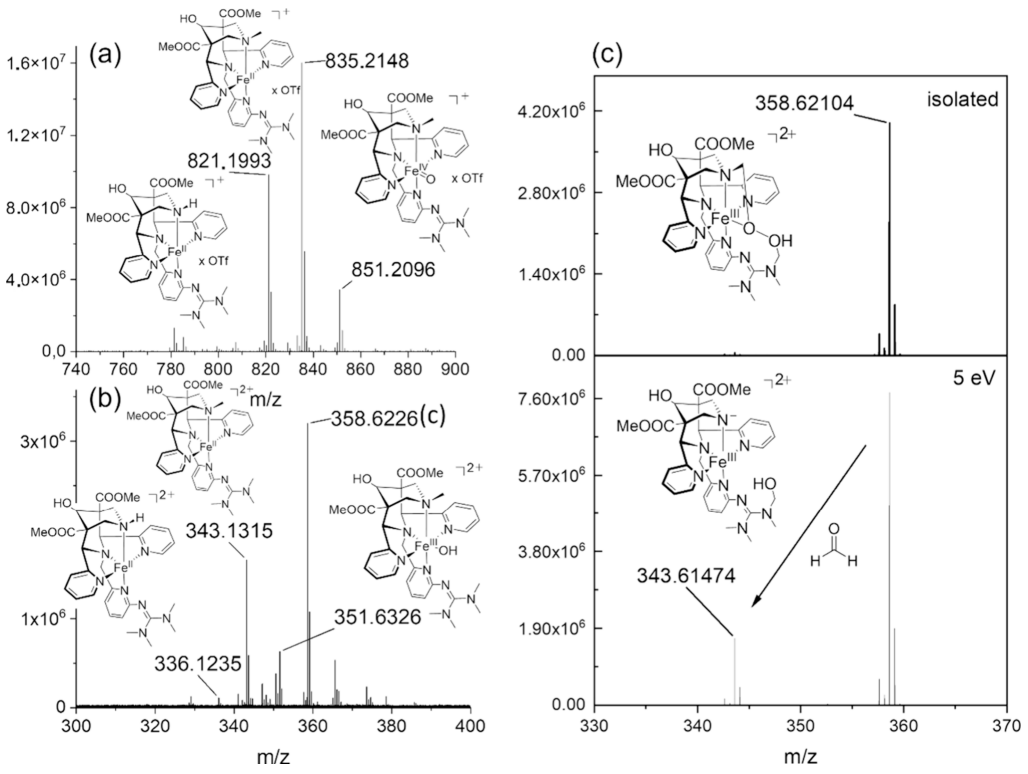

Figure 2. HR-ESI-MS of 10^{-5} M $[(L^1)Fe^{II}(NCMe)]^{2+}$ (MeCN, 3 eq ^{s}PhIO, positive mode), see also Table S3 (note that the structures given in this figure are assumptions that are further supported by spectroscopy and product analysis, see text); (a) m/z range 740−900: 821.1993: $[L^1{}_{-CH2}Fe^{II}]OTf^+$ (*D* in Scheme 2); 835.2148: $[(L^1)Fe^{II}]OTf^+$ (*A* in Scheme 2); 851.2096: $[(L^1)Fe^{IV}{=}O]OTf^+$ (*B* (or *E*) in Scheme 2); (b) m/z range 300−400: 336.1235: $[(L^1{}_{-CH2})\ Fe^{II}]^{2+}$ (*D* in Scheme 2); 343.1315: $[(L^1)Fe^{II}]^{2+}$ (*A* in Scheme 2); 351.6326: $[(L^1)Fe^{III}(OH)]^{2+}$; 358.6226: $[(L^1{}_{-H})Fe^{III}OO]^{2+}$ (derivative of *H* in Scheme 2; species (c), see tandem MS); (c) tandem ESI-MS of the postulated peroxido species with a mass of 358.62190 (positive mode) with an accelerating voltage of 5 V, complex fragments via formaldehyde cleavage. For each sum formula, the corresponding assumed structure is shown; see the Supporting Information for details—this also includes the simulation of the most important species, Figure S21.

quadrupole doublets (Figure 1d), where the third doublet with $\delta = 0.51$ mm s^{-1} and $|\Delta E_Q| = 0.45$ mm s^{-1} is typical for a high-spin Fe^{III} species.

The experimental spectroscopic data are well reproduced by the quantum-chemical calculations discussed ahead, see Table 1, and therefore fully support the structures of important intermediates of the proposed mechanism.

The formation of an Fe^{III}-peroxido species by OAT from ^{s}PhIO to an Fe^{II} precursor in water-free and strictly anaerobic conditions is unexpected, unique, and therefore of immense interest. In the following sections, we will present and discuss the mass spectrometric and spectroscopic data and mechanistic analysis together with a thorough computational analysis in support of the proposed consensus mechanism for O−O bond formation. This will be followed by a critical discussion of the proposed overall mechanistic scenario and the question whether there are realistic alternative mechanistic pathways.

From the time-resolved UV−vis−NIR spectra of reactions at low temperature, where it is possible to trap and characterize an iron(IV)-oxido intermediate, it emerges that the Fe^{III}−OOR formation is preceded by Fe^{IV}=O formation (Figure 1b, Figures S3, S4), followed by its decay to an Fe^{III}-peroxido species. Formally, OAT to Fe^{IV}=O may produce an Fe^{III}-superoxido intermediate—note that such species are extremely reactive and of interest in oxygen activation.[49−55] Formation of Fe^{III}-superoxido/peroxido species from Fe^{IV}=O in excess ^{s}PhIO has not been observed so far, specifically not in any of our work with L^3, L^4, and L^5, where we generally use excess ^{s}PhIO to obtain quantitative formation of the ferryl species.[31−33] It therefore appears that another mechanism is responsible for the formation of the O−O bond.

To further investigate the formation and reactivity of L^1-derived Fe^{III}-superoxido, -peroxido, and Fe^{IV}=O species, we have used mass spectrometry to study the oxidation of $[(L^1)Fe^{II}(NCMe)]^{2+}$ with ^{s}PhIO, and we have also studied the OAT reactivity to thioanisole of the Fe^{IV}=O and Fe^{III}-peroxido oxidants kinetically and by product analyses.

Mass Spectrometric Analyses of the Fe^{III} and Fe^{IV} Species. Mass spectrometry (MS) is unique among the techniques for the characterization of reactive intermediates by providing information on their stoichiometry.[32,56] The MS analysis reported here was inspired by the observation and thorough analysis of intramolecular C−H abstraction processes in highly reactive bispidine-Fe^{IV}=O complexes.[32,56] The spectra of relevant ESI-MS experiments are shown in Figure 2 (the Supporting Information contains further spectra, a list of all observed species, and the comparison of experimental and simulated MS of the most important intermediates, Table S4, Figures S10−S21). Note that MS does not provide structural information, and the structures given in Figure 2 are not more than educated guesses that, however, are further supported by other spectroscopic techniques and product analyses (vide infra). Support for the initial fast formation of Fe^{IV}=O emerges from Figure 2a. At rt, there is fast decay of this $S = 1$ ferryl complex, and we therefore have not been able to trap and unambiguously characterize it by Mössbauer spectroscopy.

https://doi.org/10.1021/acs.inorgchem.5c01373
Inorg. Chem. 2025, 64, 17672−17686

Scheme 2. Proposed Mechanism of the Formation and Decay of Various $Fe^{II/III/IV}$ Species[a]

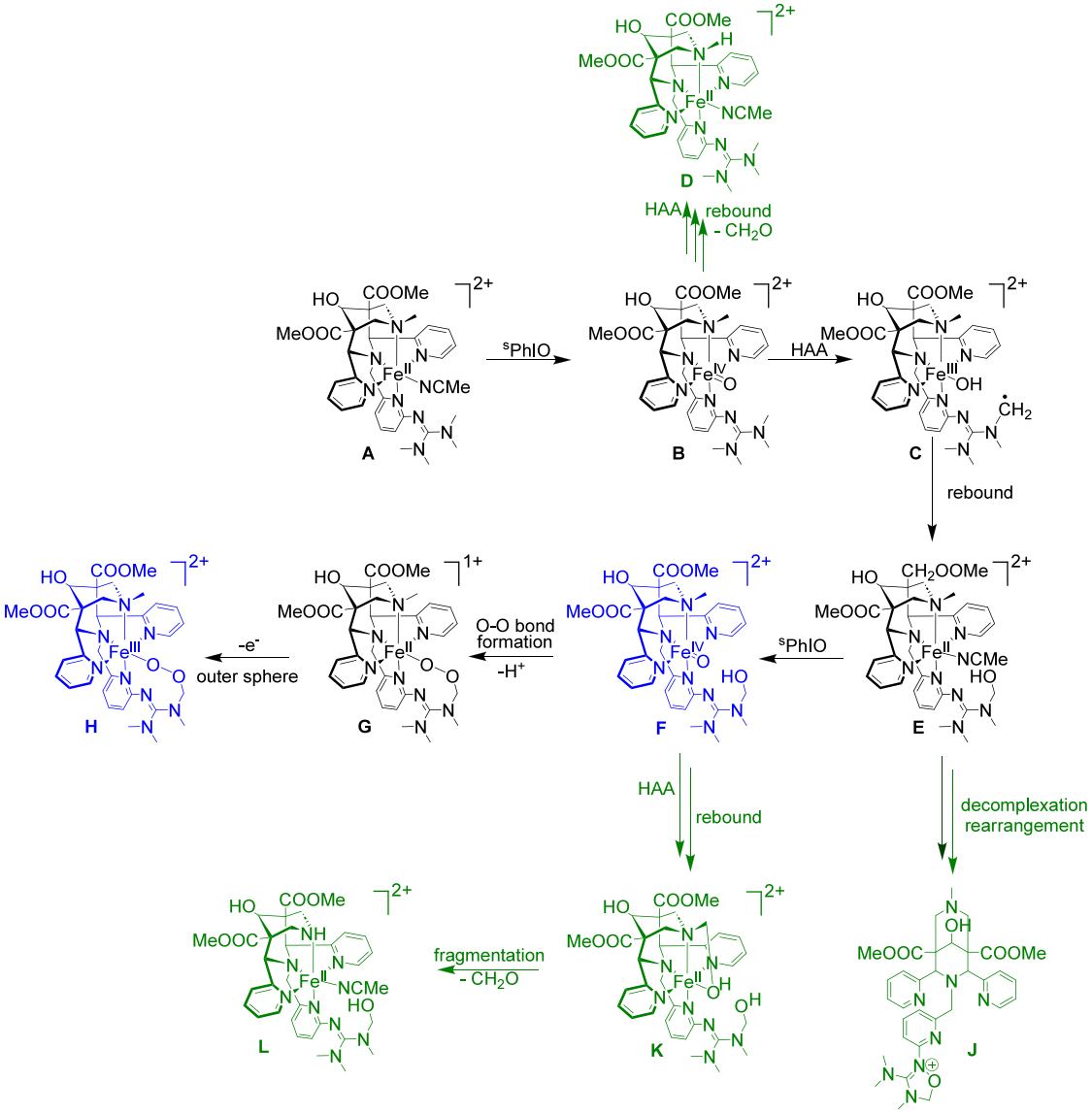

[a]The major pathway is in black/blue, the side reactions are in green, and the blue structures are the intermediates of main interest. Coordination spheres are generally completed to octahedral by the solvent NCMe. The oxido species *B* and peroxido species *H* are the oxidants for thioanisole. The stoichiometries of *A*, *B*, *H*, and *J* are supported by ESI-MS, *L* is supported by tandem ESI-MS, and *B* and *H* are supported by various spectroscopies (see text). Protonation/deprotonation processes at some of the species (e.g., *G*, *H*) are ignored in this scheme (see text).

The MS data indicate that, similar to other ferryl systems,[32,56,57] $[(L^1)Fe^{IV}{=}O]^{2+}$ (*B* in Scheme 2) decays via intramolecular HAA to the Fe^{III}−OH/radical intermediate *C*, followed by a rebound step forming the Fe^{II}−NCMe species *E* with a hydroxylated guanidinyl substituent. That HAA preferentially occurs at the guanidinium group (vide infra for the alternative HAA at the methyl group at N7) is supported by (i) the observation by HR-ESI-MS of signals assigned to metal-free ligand derivatives with heterocyclized oxygenated guanidine groups (*J* in Scheme 2, Figure S20) and (ii) the formation of an iron(III)-peroxido species (Figure 2b, species (c) and its decay path in tandem MS, Figure 2c) and the support of its electronic structure by various spectroscopies and their computational analysis (Figure 1, Table 1).

Proposed Mechanism for the Formation of the Fe^{III}-Peroxido Species. With an excess oxidant, the Fe^{II} rebound product *E* is expected to be reoxidized to Fe^{IV}=O complex *F*. This is well preorganized for the formation of an O−O bond, involving the Fe^{IV}=O and OH-substituted guanidinyl groups, to form the Fe^{II}-peroxido intermediate *G* (Scheme 2). We were not able to trap and characterize *G* because its formation must be slower than its decay to *H*, presumably by an outer-sphere electron transfer with excess ^{s}PhIO. Support for the proposed mechanism emerges from spectroscopy (UV−vis−NIR, EPR, Mössbauer, see Figure 1) and reactivity studies (formation of *H* followed by OAT to thioanisole, see below). In addition, products of the intramolecular decay of *F* have been observed by MS: in an intramolecular HAA species, *F* abstracts a hydrogen atom of the methyl group at N7, producing a short-lived Fe^{II}-hydroperoxido/radical intermediate, followed by rebound and loss of CH_2O (Figure 2c, species *L*). Similar decay reactions have been studied experimentally and by computational analyses with the tetradentate bispidine L^5 and for other systems.[32,56,57] Note that only traces of the

https://doi.org/10.1021/acs.inorgchem.5c01373
Inorg. Chem. 2025, 64, 17672−17686

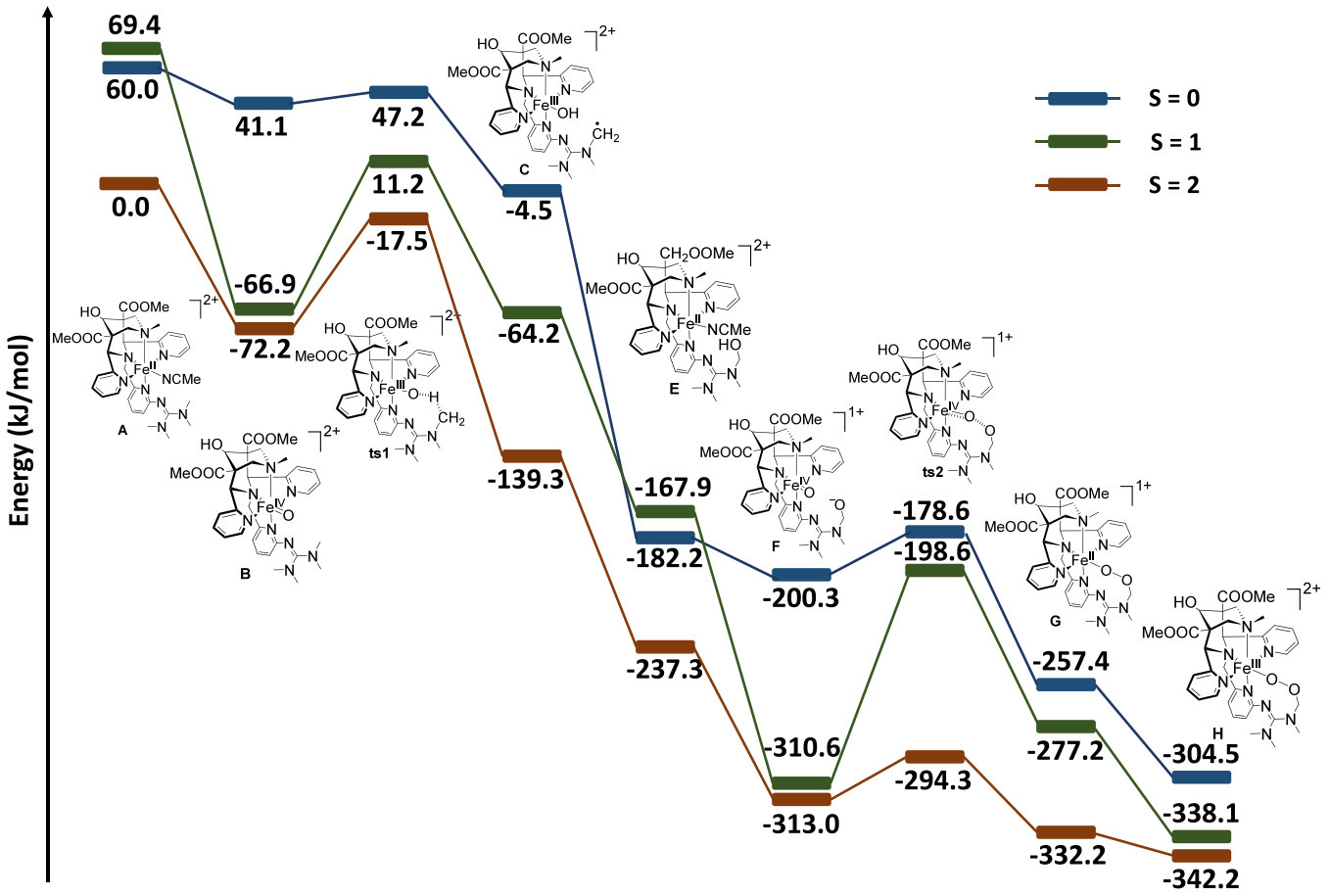

Figure 3. Computed potential energy profile diagram in the solvent phase, with free energies (ΔG in kJ/mol), at the B3LYP-D3/def2-TZVP level of theory for the reaction involving the O−O bond formation in the coordination sphere of a bispidine-iron(IV)-oxido complex, see also the Supporting Information, Table S6.

intramolecular HAA product *D* were observed (demethylation of *B* at N7, minor signal at m/z = 336.1235 in Figure 2b, i.e., the preferred decay path of *B* is to C).

Importantly, therefore, the major decay pathway of the ferryl species *B* is an intramolecular HAA at the guanidinyl substituent, i.e., formation of *E* and the follow-up products *F*, *G*, and *H* is very efficient. Trapping of the radical intermediate *C* with CCl_3Br (100 eq vs. precursor *A*, see the SI) was unsuccessful.[55,58−60] Fe^{III}−OH/radical intermediates of HAA initiated by Fe^{IV}=O species generally react via radical rebound or "cage escape", where the radical diffuses to the solvent or a radical scavenger (e.g., O_2 or an added radical trap, such as CCl_3Br) enters the cage to compete with the rebound path. Since the radical in *C* is ligand-based, diffusion to the solvent ("cage escape") is prevented, and the ligand-enforced preorganization of the Fe^{III}−OH···$^{\cdot}CH_2$−guanidinyl unit instigates a very short lifetime of the intermediate, avoiding reaction with an external radical trap. Therefore, *C* is an extremely short-lived species and an excellent example of rebound in nonheme iron model systems.

Time-resolved UV−vis−NIR spectroscopy indicates that formation of the Fe^{III}-peroxido complex *H* is a fast reaction under the standard condition of our experiments (0.5 mM $[(L^1)Fe^{II}(NCMe)]^{2+}$ in MeCN, 0.8−3 eq ^{s}PhIO, Ar, rt) with a half-life of approximately 3 min (Figure S3). This is a complex multiphase reaction, and a quantitative analysis of the kinetics is therefore not appropriate. Since the key intermediate *G* is too short-lived for trapping and spectroscopic analysis, we now turn to a thorough DFT-based quantum-chemical analysis of the entire reaction sequence. Let us first briefly reiterate the evidence emerging from the experiment: (i) Oxidation of precursor $[(L^1)Fe^{II}(NCMe)]^{2+}$ *A* with ^{s}PhIO produces the ferryl complex $[(L^1)Fe^{IV}{=}O]^{2+}$ *B* (various spectroscopies, OAT reactivity). (ii) In an excess of the external oxidant ^{s}PhIO, this produces the Fe^{III}-peroxido complex *H* (various spectroscopies, MS, OAT reactivity). (iii) Under the conditions of the experiment, the only oxygen source is ^{s}PhIO. (iv) Hydroxylation of a guanidinyl methyl group emerges from MS.

Mechanistic Insights on the O−O Bond Formation via Computational Analysis. The mechanism derived from experiments (Scheme 2) was analyzed by DFT-based quantum-chemical methods as illustrated in Figure 3 (Supporting Information, Scheme S2). The reaction is initiated by the oxidation of the precursor $[(L^1)Fe^{II}(NCMe)]^{2+}$ (A) with ^{s}PhIO, resulting in the exothermic formation of the Fe^{IV}=O species *B* (−72.2 kJ/mol) with a quintet ground state and the triplet only 5.3 kJ/mol higher (note that experimentally, a triplet ground state is observed, see above Figure 1, and by DFT the triplet and quintet states are within the error limit degenerate, since relatively large error limits for spin state energies of ferryl complexes are a common problem;[47] for the analysis reported here, this, however, is not a significant drawback). The formation energy of an Fe^{IV}=O species from an Fe^{II} precursor using a strong oxidant

https://doi.org/10.1021/acs.inorgchem.5c01373
Inorg. Chem. 2025, 64, 17672−17686

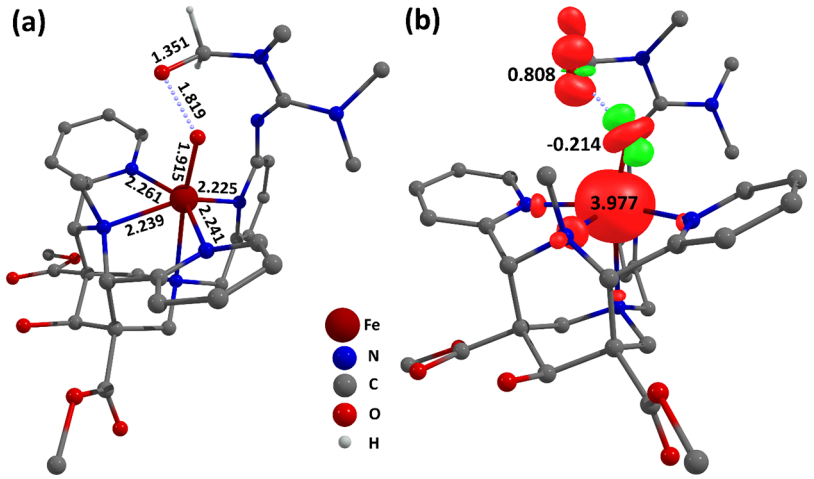

Figure 4. DFT-computed structure of ts2 (O−O bond formation, ground spin state): (a) selected bond parameters and (b) spin density plot; radical−radical coupling mechanism at the B3LYP-D3/def2-TZVP level of theory (most hydrogen atoms are omitted for clarity).

depends on the ligand environment, spin state, and solvent. For systems with similar nitrogen-based ligands, DFT studies typically estimate the reaction free energy in the similar range of −20 to −50 kJ/mol.[61,62] From species *B*, there are two possible routes for hydrogen atom abstraction (see Scheme 2): in pathway *a*, an intramolecular ligand oxidation reaction occurs, starting with the oxido group of species *B* abstracting a hydrogen atom from the guanidine pendant group via transition state ts1 with an energy barrier of 54.7 kJ/mol (imaginary frequency i1804 cm^{-1}), leading, in an exothermic reaction, to the Fe^{III}−OH species *C* with an appended guanidinyl radical in the quartet state at −139.3 kJ/mol. There are two distinct transition state pathways for HAA by Fe^{IV}=O species *B*: the σ- and the π-pathways. In the present case, the electron is accepted by the π^* (d_{xz}) orbital of Fe, with a computed Fe−O−H angle of 127.3°, characteristic of a π-pathway. The σ-pathway would lead to a linear Fe−O···H arrangement (electron transferred to the σ^* (d_{z2}) orbital), and this is prevented by constraints imposed by the ligand backbone, i.e., the methyl group of the guanidinyl donor approaches the Fe^{IV}=O center through a bent rather than a linear geometry, viz., the ligand architecture inherently enforces the π-pathway for the HAA step. Subsequently, an intramolecular radical rebound occurs without any energy barrier (radical rebound barriers are generally very low and not often resolved[61]—in the present example, cage escape is prevented since the radical is ligand-appended, see above). The radical rebound step results in the exothermic formation of species *E* at −98 kJ/mol from *C*.

From the ferryl species *B*, there is an alternative intramolecular C−H activation pathway *b*, i.e., HAA at the methyl group of N7 (formation of species *D*, see Scheme 2), which has a high energy barrier of 73.2 kJ/mol (imaginary frequency i2032 cm^{-1}), nearly 20 kJ/mol less favorable than pathway *a*, and this therefore is ruled out (vide supra for the corresponding discussion of the experimental data). The oxidation of *E* with ^{s}PhIO leads to the exothermic formation of ferryl species *F* at −75.7 kJ/mol from *E*. In the next step, *F* undergoes very efficient O−O bond formation via ts2, with an energy barrier of only 18.7 kJ/mol (imaginary frequency i629 cm^{-1}) from *F*, resulting in the Fe^{II}-peroxido intermediate *G*. Following this, an outer-sphere electron transfer occurs, leading to the exothermic generation of the final Fe^{III}-peroxido species *H*. As illustrated in the potential energy surface scheme in Figure 3, the overall reaction, starting from Fe^{II} precursor *A*, is exothermic all the way up to species *H*, and the computed kinetic barriers are more than compensated by the thermodynamic stability of the various species, suggesting a facile formation of the O−O bond, once the Fe^{II} precursor is oxidized. The entire reaction is found to occur on the quintet spin surface without any need for energy consuming spin crossing, making the reaction all the more facile as observed experimentally.

Electronic Structural Aspects of the O−O Bond Formation. High-valent metal-oxido species are known to facilitate O−O bond formation via various possible mechanistic pathways, including single-electron-transfer−water-nucleophilic-attack (SET-WNA), direct water nucleophilic attack (WNA), and radical-mediated coupling, involving metal-oxyl and oxygen-centered radicals.[13,63,64] A detailed electronic structure analysis of the Fe^{IV}=O species *F* indicates that O−O bond formation proceeds via an oxygen-centered radical−radical coupling mechanism (see Figure 4). In the transition state, the nucleophilic $-CH_2O^-$ fragment attacks the Fe^{IV}=O center, and spin density builds up on its oxygen atom (0.808), while the Fe^{IV}=O moiety shows a complementary spin polarization (−0.214). This suggests partial radical character on both oxygen atoms, facilitating the coupling pathway. The computed spin density distribution at the transition state supports a singlet O−O bond formation with a $[Fe^{III\uparrow}\text{-}O^{\downarrow}\text{-}O^{\uparrow}\text{-}R]^{1+}$ pattern (see Figure 4), characteristic of a radical-type coupling process. The computed O···O distance is 1.819 Å at the O−O coupling transition state with an imaginary frequency of i629 cm^{-1} (Figure 4a). A frontier molecular orbital (FMO) analysis indicates that the key orbital interaction responsible for the formation of the O−O bond is between the singly occupied $(\pi^*)^1_{Fe(IV)=O}$ and $(\pi^*)^1_{O\text{-}radical}$ orbitals (see below). The Fe^{IV}=O species possesses an antibonding π^* orbital that is primarily localized on the oxido ligand, with a significant contribution from the Fe d_{yz} orbital. Similarly, the ligand-based oxygen radical has an unpaired electron in an π^* molecular orbital (π^*_O). The interaction between these two singly occupied π^* orbitals leads to the constructive overlap of their respective wave functions that is responsible for the efficient radical coupling. This overlap facilitates electron delocalization

https://doi.org/10.1021/acs.inorgchem.5c01373
Inorg. Chem. 2025, 64, 17672−17686

Table 2. Kinetics of the Sulfoxidation of Thioanisole by $[(L^1)Fe^{IV}{=}O]^{2+}$ (Oxido, See Text), $[(L^1)Fe^{III}OOR]^{2+}$ (Peroxido, See Text), and Analogues with L^2, L^3, and L^4 (MeCN, 25 °C, Ar) and Yields of Catalytic Reactions[a]

complex	OAT by	k_2 [M^{-1} s^{-1}]	yield [%]
$[(L^1)Fe^{II}(NCMe)]^{2+}$	oxido complex	17.9 ± 4.9	25 ± 4
$[(L^1)Fe^{II}(NCMe)]^{2+}$	peroxido complex	(2.25 ± 0.50) × 10^{-2}	37 ± 14
$[(L^2)Fe^{II}(NCMe)]^{2+}$[42]	oxido complex	69.7 ± 0.6	60.0 ± 0.8
$[(L^3)Fe^{II}(NCMe)]^{2+}$[42,76]	oxido complex	5.65 ± 0.1[b]	56.2 ± 6.7
$[(L^4)Fe^{II}(NCMe)]^{2+}$ [76]	oxido complex	129 ± 2	73
blank			4 ± 1

[a]% with respect to the oxidant. Fe^{II} 5 mM in MeCN, 25 °C, Ar; catalyst: ^{s}PhIO (oxidant): substrate = 1:20:100; workup after 1 h, see the SI for details and additional data; the yield for the reaction with the peroxido complex emerges from a reaction where the catalyst and the oxidant were mixed and stirred for 10 min prior to the reaction with thioanisole. [b]Ketone/hydrate at C9.[42,65]

and subsequent bond formation, resulting in the O−O bond through a σ-type interaction.

A frontier molecular orbital analysis (FMO, see the Supporting Information) of the O−O bond formation transition state (ts2) reveals key contributions from the oxygen atoms involved in bonding. A Mulliken population analysis shows that in the α-spin HOMO, the contributions of O1 and O2 are 8% and 9%, respectively, while in the β-spin HOMO, their contributions increase to 10.2% and 12.0%. This indicates an active participation of both oxygen atoms in the molecular orbitals, particularly in the β-spin channel, reflecting spin polarization and supporting their key role in the O−O bond formation (see Figure S42).

The formation of the O−O bond is supported by experiments, including UV−vis, EPR, and Mössbauer spectroscopies (see above), as well as the observed OAT reactivities of both $Fe^{IV}{=}O$ *B* and Fe^{III}−OOR *H* species, which are, as expected, very different (see below). The computed TD-DFT and Mössbauer parameters are in excellent agreement with the experimental data (see Table 1), providing a strong validation for our computational and experimental findings and reinforcing the proposed O−O bond formation mechanism. Overall, these results highlight the role of orbital symmetry and radical localization in driving very efficient O−O bond formation in high-valent iron-oxido species.

Oxidation of Thioanisole: Kinetics, Catalysis, and Computational Analysis. Bispidine-based $Fe^{IV}{=}O$ complexes are very reactive and efficient oxidants and oxidation catalysts. With the two isomers L^3 and L^4 (see Scheme 1), the latter forms the more reactive ferryl complex, but the former is still able to efficiently oxidize cyclohexane.[30,65] The sulfoxidation of thioanisole is a routinely studied and biologically, environmentally, and technically important oxidation reaction of nonheme iron oxidants with a significant amount of published experimental work supported by extensive computational studies.[30,66−68] In a recently reported series of ferryl complexes with derivatives of L^4, all had second order rates for the sulfoxidation of thioanisole (OAT, MeCN, 25 °C, Ar) in the order of 1−100 $M^{-1}s^{-1}$.[42] Here, we concentrate on the OAT reactivity of the $[(L^1)Fe^{IV}{=}O]^{2+}$ species *B* in comparison to the $[(L^1)Fe^{III}$−OOR$]^{2+}$ species *H*. The observed rates and product yields (Table 2) support the pathways proposed in Scheme 2 and are supported by the computational study above with the enormous and expected reactivity differences between the oxido and peroxido oxidants. The detailed computational analysis of OAT to thioanisole agrees with the observed reactivities: the calculations reveal that the barrier for the reaction with $[(L^1)Fe^{IV}{=}O]^{2+}$ (*B*) of 56.5 kJ/mol (imaginary frequency i326 cm^{-1}; see the Supporting Information for a tabulation of all important energies and energy barriers) is very low (see Figure 5), whereas for the reaction with the peroxido complex $[(L^1)Fe^{III}$−OOR$]^{2+}$ (*H*), the energy barrier of 95.2 kJ/mol (imaginary frequency i289 cm^{-1}) is substantially higher (see the Supporting Information, Figure S38, Table S6). In the case of OAT with $[(L^1)Fe^{IV}{=}O]^{2+}$ (*B*), the spin crossover occurs prior to the transition state, leading to a point where the energies of the quintet and triplet states intersect (minimum energy crossing point, MECP).[69] The computed energy of the MECP is 49.2 kJ/mol lower than the computed OAT transition state barrier of 56.5 kJ/mol. This indicates that the kinetic barrier for the reaction is governed by the transition state of the OAT and not by the spin crossover event. Therefore, the DFT analysis suggests that the ferryl species *B* is a very efficient oxidant, while the OAT process initiated by the peroxide species *H* is comparably sluggish. This aligns very well with the experimental observations; i.e., $[(L^1)Fe^{IV}{=}O]^{2+}$ is much more reactive than $[(L^1)Fe^{III}$−OOR$]^{2+}$ (see Table 2).

Moreover, the observed and computationally predicted reactivities are as expected from published studies: Fe^{III}-peroxido complexes are known as sluggish oxidants, and only a few examples with appreciable reactivity have been reported.[55,70−74] In one recent example, an Fe^{III}-alkylperoxido complex supported by a pentadentate bispidine with hydrogen bond donor groups has been shown to sulfoxidize thioanisole. A combination of experiments and computational work revealed however that the reactivity was due to O−C bond cleavage, i.e., OAT to the thioether occurred from an Fe^{III}-superoxido complex.[55] We therefore tested the OAT of *H* in the presence of excess CCl_3Br.[55,58−60] The fact that no trace of any brominated product was detected indicates that the reactivity of *H* is not due to the formation of an Fe^{III}-superoxido species.

In another recent publication on tetramethyl-substituted tetraaza macrocycles (12-, 13-, and 14-membered TMC derivatives), with a combination of reactivity studies, spectroscopy, and computational work, it was shown that the change of reactivity along the series is due to a valence tautomer with Fe^{II}-superoxido character, which was most pronounced with the smallest macrocycle.[55,70,71] With the 14-membered TMC based peroxido complex, in earlier work, it was shown that this complex is able to oxidize thioanisole, and the reactivity was shown to be due to heterolytic O−O bond cleavage, leading to a particularly reactive $Fe^{V}{=}O$ species.[72] The significant difference between these two studies with TMC-based ligands and our system reported here is that the former includes high-spin Fe^{III}-peroxido complexes,[71,72] while the preferential spin state of *H* is low-spin (Figure 1). Low-spin

https://doi.org/10.1021/acs.inorgchem.5c01373
Inorg. Chem. 2025, 64, 17672−17686

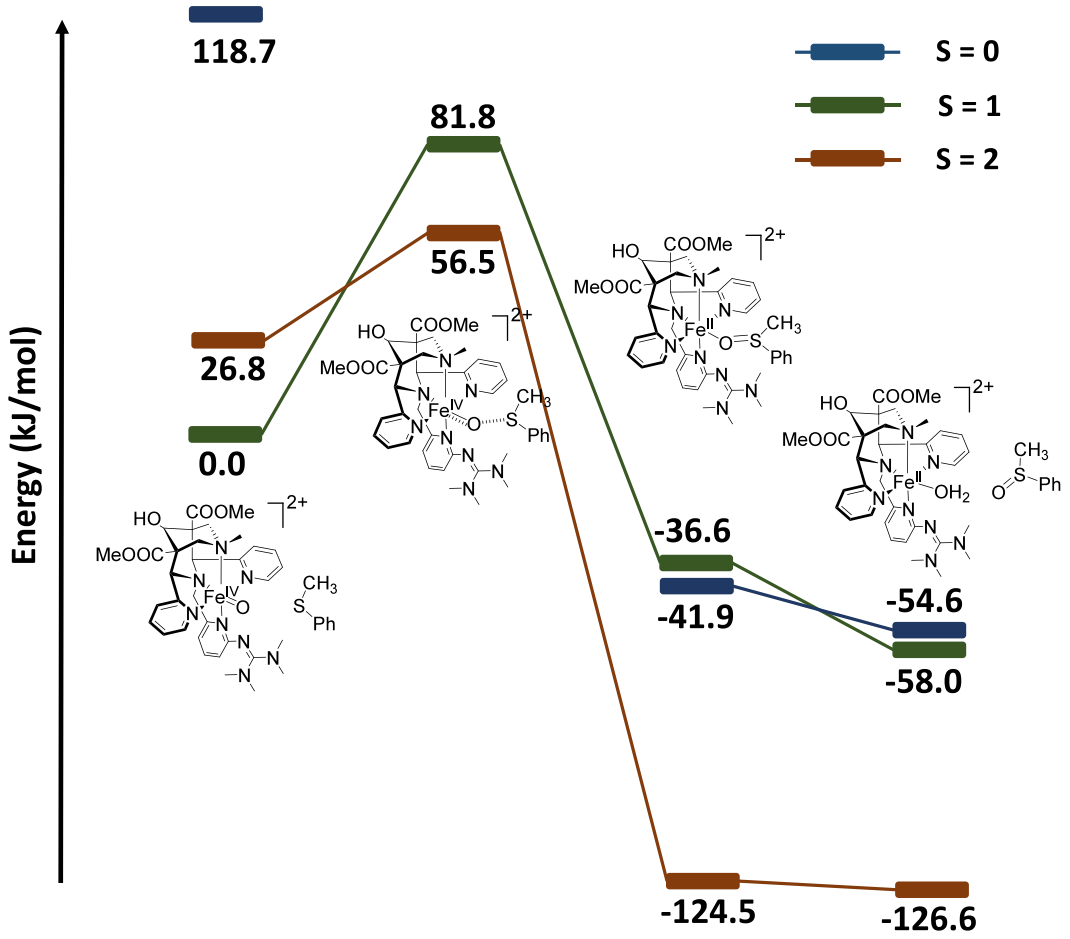

Figure 5. Computed potential energy profile diagram in the solvent phase, with free energies (ΔG in kJ/mol) at the B3LYP-D3/def2-TZVP level of theory for OAT involving thioanisole and $[(L^1)Fe^{IV}{=}O]^{2+}$ (*B*), see also the Supporting Information, Table S6.

Fe^{III}-peroxido complexes are known to react via homolysis, and this has been shown for all bispidine systems studied so far.[44,75]

It is interesting to compare the $[(L^1)Fe^{III}{-}OOR]^{2+}$ pathway discussed here with the recently reported Fe^{III}-superoxido based sulfoxidation of thioanisole, studied with a structurally similar pentadentate bispidine.[55] The second order rate constant under similar conditions as used here was 7.8×10^{-2} M^{-1} s^{-1}, i.e., comparable to the rate observed here (entry 2 in Table 2). Based on a DFT analysis, the observed rate in the earlier example was due to a relatively sluggish formation rate of a very reactive superoxido species; i.e., the activation barrier for the O−C cleavage was calculated to be 70 kJ/mol, while the barrier for the OAT was only 40 kJ/mol. There is no information so far on whether the OAT by $[(L^1)Fe^{III}{-}OOR]^{2+}$ is a concerted or stepwise reaction and whether possibly O−O cleavage is rate limiting. Formally, the iron-based product of the OAT is an Fe^{II} complex with a guanidinyl-centered oxygen radical. A $1e^-$ reduction then formally closes the catalytic cycle to species *E*.

Notably, the yield of the catalytic formation of methyl-phenylsulfonate (MPSO) in the current system is largely independent of whether the reaction is initially based on Fe^{IV}-oxido species *B* or Fe^{III}-peroxido oxidant *H*. While one needs to be cautious in the interpretation of these observations, the data in Table 2 are in full agreement with the mechanistic proposal in Scheme 2, which is also supported by computational analysis.

Are There Alternatives to the Proposed Mechanism?

The O−O bond formation in the coordination sphere of an $Fe^{IV}{=}O$ species, the essential initial step in water oxidation, is the focus of the present communication. The key species is the iron(III)-peroxido complex $[(L^1)Fe^{III}{-}OOR]^{2+}$ (*H*). Our data discussed in detail above provide a robust basis for the interpretation summarized in Scheme 2. However, as usual with mechanistic work, it is important to consider alternatives. The central observations that fit the proposed mechanistic scenario and need to fit any alternative are as follows: (i) Mass spectrometry indicates that the initially formed iron(IV)-oxido species (corroborated by electronic spectroscopy) decays by intramolecular HAA forming a hydroxylated guanidinyl methyl group as the major product. (ii) Mass spectrometry of the final decay product *H* defines it as an iron complex of L^1 with two additional oxygen atoms, i.e., one in addition to the hydroxylated ligand; from EPR and Mössbauer spectroscopy, it emerges that *H* is an iron(III) complex close to the spin crossover limit, i.e., dependent on temperature and protonation degree (*H* can be reversibly protonated), the hs/ls ratio varies. (iii) Importantly, *H* shows an intense CT transition at around 600 nm, reminiscent of iron(III)-peroxido complexes. Mössbauer and EPR spectra are also compatible with the assignment to iron(III)-peroxido species, and importantly, this is supported by the comparison with spectroscopic signatures obtained from genuine iron(III)-peroxido, -hydroperoxido, and -^{t}Bu-peroxido complexes of the L^1-iron system, prepared independently. (iv) *H* is a competent oxidant that catalyzes

https://doi.org/10.1021/acs.inorgchem.5c01373
Inorg. Chem. 2025, 64, 17672−17686

OAT to thioanisole, albeit 2 orders of magnitude less efficiently than the original ferryl complex *B*.

An alternative for *H* to a peroxido complex is a hydroxido/aqua species: this would be consistent with the MS data and could be reversibly protonated. These iron(III) complexes would also be expected to be close to the spin crossover [(i) and (ii)]. However, the spectroscopic properties would not be expected to match those observed and modeled successfully by quantum chemical methods (see Table 1). Especially, aqua- and hydroxido complexes of iron(III)-amine-pyridine complexes do not show the strong CT bands observed for the peroxido complexes. Importantly, aqua- (and hydroxido)iron-(III) complexes are expected to show fast solvent exchange, i.e., under conditions of the experiments, they would decay fast to the corresponding acetonitrile complexes, and these would be expected to have a low spin electronic configuration and not show any proton-dependent equilibria. Importantly, the aqua/hydroxido complexes would therefore not be expected to be competent oxidants for OAT to thioanisole.[55]

Therefore, the combination of all experimental data (mass spectrometry, spectroscopy, kinetics, and OAT reactivity) indicates that there is an O−O bond formation to a peroxide species, and this is fully supported by the DFT-based mechanistic analysis of the O−O bond formation by computational spectroscopy and the computational analysis of the OAT reactivity of both the initial ferryl complex and its peroxide decay poduct.

CONCLUSIONS

The two most relevant and exciting results of the oxidation of $[(L^1)Fe^{II}(NCMe)]^{2+}$ with excess ^{s}PhIO (MeCN, 25 °C, water- and oxygen-free) are as follows: (i) the main product is an Fe^{III}-alkylperoxido complex, where the alkyl-group is part of the ligand—importantly, this implies O−O bond formation in the coordination sphere of this nonheme iron model system—and (ii) the resulting Fe^{III}-peroxido complex is an efficient oxidant for the OAT to thioanisole. The proposed mechanism for the O−O bond formation is based on a thorough ESI-MS/tandem-MS study for the analysis of the stoichiometries of the various species, supported by UV−vis−NIR, EPR, and Mössbauer spectroscopies to define the oxidation and spin states of the various iron species of interest. This is supported by kinetics and product analyses of the OAT reaction of the iron(IV)-oxido and iron(III)-peroxido intermediates with thioanisole as a substrate. DFT analyses of the pathways and the spectroscopic properties of the various iron-based intermediates fully support the interpretations of the experimental findings. Key features are that the intramolecular HAA at the guanidinyl pendant group of the ligand is the preferred pathway due to preorganization of the hydrogen atom abstraction site with respect to the Fe^{IV}=O oxidant, and the Fe^{III}−OH/radical intermediate reacts for the same reason (preorganization) solely via radical rebound. Again, due to efficient preorganization, the reoxidized Fe^{IV}=O intermediate with a hydroxylated ligand reacts under O−O bond formation to the Fe^{III}-peroxido product. It appears that the intramolecular HAA is rate limiting, and the O−O bond formation is a very efficient reaction: at ambient temperature, the entire reaction cascade has a half-life of only a few minutes. All experimental observations and kinetics are supported by in-depth DFT calculations. Importantly, these reveal that the O−O bond formation proceeds on the quintet surface with very low barriers, paving a possible way forward for a novel technique to generate oxygen evolving reactions (OER) using high-valent Fe^{IV}=O species.

EXPERIMENTAL SECTION

Materials and Methods. All chemicals and reagents were purchased from commercial sources (ABCR, ACROS, Sigma-Aldrich, and TCI). Dry solvents were stored over molecular sieves and used without further purification. Air-sensitive materials were prepared and handled using either Schlenk techniques or a glovebox under an Ar atmosphere. L^2, L^3, and L^4, activated urea and ^{s}PhIO were prepared as described before.[42,77−79] Spectra were analyzed with OriginPro 2020.

MS experiments were carried out on an ApexQe hybrid 9.4 T FT-ICR instrument from Bruker. For HR-ESI-MS measurements, the samples were prepared in the glovebox. The measured solutions had iron complex concentrations of 1×10^{-5} M in abs. MeCN to which the required amounts of oxidant were added. The reactions were carried out in a total reaction volume of 2 mL. The reactions were stirred 1 h at rt before 1 mL of the reaction solution was taken, filtered through a syringe filter and filled into a vial with septum. Tandem-MS studies were performed on a timsTOFfleX mass spectrometer from Bruker. For the measurements, solutions with 10^{-5} mol L^{-1} complex in MeCN were used. As the ionization method, ESI in positive mode was used. Collision-induced dissociation was performed with argon as collision gas. The isolation window was set to 1−5 m/z as required. The collision offset voltage was increased stepwise during the measurement, starting from 5 to 15 V. For each measured spectrum, up to 14 individual measurements were combined and the average was reported. The measurements were carried out by the Mass Spectrometry Facility, Department of Chemistry, Heidelberg University.

Elemental analyses were performed on a CHN-O Vario EL by the "Mikroanalytisches Labor", Department of Chemistry, Heidelberg University.

UV−vis−NIR spectra were recorded on an Agilent 8453 spectrophotometer equipped with a USP-203-A cryostat from Unisoku.

^{57}Fe Mössbauer spectra were recorded on an alternating constant-acceleration spectrometer. The minimal line width was 0.24 mm s^{-1} full width at half-height. The sample temperature was maintained constant in a bath cryostat (Wissel MBBC-HE0106). ^{57}Co/Rh was used as the radiation source. Isomer shifts were determined relative to those of α-iron at room temperature.

EPR spectra were recorded on a Bruker ELEXSYS-E500 instrument. The measurements were made in vertical mode at the X-band (microwave frequency 9.63461−9.63691 GHz) under helium cooling.

NMR spectra were recorded at 400 MHz (^{1}H) and 101 MHz (^{13}C) on Avance II or at 600 MHz (^{1}H) and 151 MHz (^{13}C) on Avance III instruments from Bruker with the solvent as an internal reference.

For X-ray crystallography, full shells of intensity data were collected at low temperature with an Agilent Technologies Supernova-E CCD diffractometer (Cu-K_α radiation, microfocus X-ray tubes, and multilayer mirror optics). Details of data collection and refinement are given in the SI.

Syntheses. *Methyl 5-Acetoxy-3-((6-((bis(dimethylamino)-methylen)amino)pyridine-2-yl)methyl)-9-hydroxy-7-methyl-2,4-di-(pyridine-2-yl)-3,7-diazabicyclo[3.3.1]nonane-1-carboxylate* L^1. L^2 (171 mg, 0.30 mmol, 10 eq) was dissolved in 10 mL of dry MeCN under inert gas. The solution was cooled to 0 °C, and activated urea (Vilsmeier salt of the methylated urea derivative) $(C_5H_{12}ClN_2)Cl$ (109 mg, 0.60 mmol, 2.0 eq) and triethylamine (325 mg, 3.00 mmol, 10.0 eq) were slowly added. The reaction solution was stirred overnight at 0 °C, and then, the solvent was removed under reduced pressure. Using 1 M HCl, the reaction solution was adjusted to pH = 2, and then, using 20% NaOH, the pH was adjusted to 14. The aqueous phase was extracted three times with DCM, the organic combined phases were dried over $MgSO_4$, and the solvent was removed in vacuo. L^1 was obtained as a yellowish solid (80 mg, 0.13 mmol, 42%). Crystals for the X-ray structural analysis were obtained by recrystallization from EtOAc.

https://doi.org/10.1021/acs.inorgchem.5c01373
Inorg. Chem. 2025, 64, 17672−17686

^{1}H NMR (600.13 MHz, MeOD, 295.2 K): δ [ppm] = 8.34 (d, J = 4.4 Hz, 2H, H_{arom}), 8.13 (d, J = 7.7 Hz, 2H, H_{arom}), 7.81 (td, J = 7.7, 1.8 Hz, 2H, H_{arom}), 7.35 (t, J = 7.7 Hz, 1H, H_{arom}), 7.24 (ddd, J = 7.5, 4.8, 1.2 Hz, 2H, H_{arom}), 6.50−6.43 (m, 2H, H_{arom}), 4.92 (s, 2H, N^3CH), 4.61 (s, 1H, CHOH), 3.60 (s, 6H, $COOCH_3$), 3.45 (s, 2H, N^3CH_2); 2.64 (s, 12H, $NC(N(CH_3)_2)_2$); 2.30 (d, J = 11.9 Hz, 2H, $N^7CH_{2,\ ax/eq}$), 2.23 (d, J = 12.0 Hz, 2H, $N^7CH_{2,\ ax/eq}$), 2.14 (s, 3H, N^7CH_3). ^{13}C NMR (150.92 MHz, MeOD, 295.2 K): δ (ppm) = 172.6, 163.3, 160.0, 155.1, 147.7, 137.0, 136.2, 124.4, 122.6, 115.6, 114.4, 70.7, 70.6, 57.9, 53.0, 51.1, 50.9, 44.8, 38.7. HR-ESI MS (pos, MeOH): $[L + H]^+$: calcd. 631.3351, obsd. 631.3354 (100%). Elem. Anal. (report no. 42971). Calcd for $[L + 1.5\ H_2O]$: C 60.25, H 6.90, N 17.04%. Obsd.: C 60.55, H 6.93, N 16.92%.

Iron Complex of L^1. $Fe^{II}(OTf)_2$ (1 mmol) was added to a solution of the bispidine ligand L^1 (1 mmol) in dry acetonitrile (5 mL) under a nitrogen atmosphere. After stirring for one night and reducing the solvent volume, the precipitated complex was filtered and dried under vacuum. Crystals of the iron complex (see structure $[(L^1)Fe^{II}(OH_2)](OTf)_2$ in Figure 1) were obtained after 2 months from a concentrated solution in MeCN at ambient temperature.

$[(L^1)Fe^{II}(NCMe)](OTf)_2$(1025.19 g/mol, $C_{37}H_{45}F_6FeN9O_{11}S_2$): HR-ESI MS (pos, MeCN): $[(L^1)Fe^{II}(NCMe)](OTf)^+$: calcd. 835.2148, obsd. 835.2148 (100%). Elem. Anal. (report no. 43614). Calcd. for $[(L^1)Fe^{II}\ (NCMe)](OTf)_2\ 2\ H_2O$: calcd.: C 41.85, H 4.65, N 11.87%. Obsd.: C 42.05 H 4.63, N 11.99%.

The ^{57}Fe complex of L^1, $[(L^1)^{57}Fe^{II}(NCMe)](OTf)_2$, was synthesized for Mössbauer spectroscopy. The ligand L^1 was reacted in a 1:1 ratio with $^{57}FeCl_2$, and the addition of AgOTf converted it into the triflate complex. $^{57}Fe^{II}Cl_2$ (0.11 mmol) was added to a solution of L^1 (0.11 mmol) in dry MeCN (2 mL) under a nitrogen atmosphere. After stirring for one night and reducing the solvent volume, the precipitated complex was filtered and dried under vacuum.

HR-ESI-MS (pos, MeCN): $[(L^1)^{57}Fe^{II}(Cl)]^+$: calcd. 722.2315, obsd. 722.2318 (78%); calcd. 800.2477, obsd. 800.2481 (100%).

AgOTf (0.2 mmol) was added to a solution of $[(L^1)^{57}Fe^{II}(Cl_2)]$ (0.1 mmol) in dry acetonitrile (2 mL) under a nitrogen atmosphere and light exclusion. After stirring for one night, the reaction solution was centrifuged and then filtered to remove AgCl. Subsequently, the solvent volume was reduced, and the complex precipitated as a yellow solid and was dried under vacuum.

HR-ESI-MS (pos, MeCN): $[(L^1)^{57}Fe^{II}](OTf)^+$: calcd. 836.2147, obsd. 836.2152 (100%). Elem. Anal. (report no. 46349). Calcd. for $[(L^1)^{57}Fe^{II}\ (H_2O)](OTf)_2$: calcd.: C 41.88, H 4.42, N 11.16%. Obsd.: C 42.32 H 4.59, N 11.13%.

Kinetics and Product Analyses. *Kinetics of Thioanisole Oxidation.* For kinetic studies of the oxido group transfer, the Fe^{II} complexes (0.5 mM, 2 mL in dry MeCN) were oxidized with ^{s}PhIO (1 eq). To this solution, different amounts of the substrate thioanisole were added. To investigate the time course of the reactions, they were followed by UV−vis−NIR spectroscopy at a constant temperature (24.8−25.2 °C). Spectra were recorded every 0.5 s and subsequently analyzed with OriginPro 2020. Each measurement was carried out at least three times, and then, the mean value of the rate constants (k_{obs}) was plotted against the substrate concentration. The second-order reaction rate constants (k_2) were determined from the slopes of the concentration-dependent rate constants. See the Supporting Information for more details and experimental data.

Product Analysis of Bulk Oxidation Reactions. For the standard conditions for the reaction with iron(IV)oxido-species, in a glovebox, a 1.5 mL glass vial was equipped with a stirring bar, 1 eq of ^{s}PhIO (9 to 12 mg), and 5 eq of substrate (17 μL of thioanisole). The reaction was started by addition of a 5 mM solution of the Fe^{II} complex (0.1 eq), dissolved in dry, absolute MeCN. The sequence of substrate addition was chosen to avoid potential side reactions and to ensure that as soon as the oxido species is formed, it can react with the substrate. The reaction was stopped after 1 h. For the workup, the vials were taken out of the glovebox after 1 h reaction time, and the solutions were filtered over a silica pipet column to separate the iron catalysts. The columns were washed with 3 mL of EtOAc, and the combined filtrate was evaporated at 40 °C. The sulfoxidation yields were determined by ^{1}H NMR spectroscopy. Therefore, 1,3,5-trimethoxybenzene (5 to 15 mg − exact amount noted) was added as internal standard to the residue, which was dissolved CD_2Cl_2. All experiments were performed twice. Yields are with respect to the used amount of oxidant. See the Supporting Information for more details.

For the standard conditions for the reaction with peroxido-compound, in order to investigate the reactivity of the peroxido compound, the procedure was slightly changed. For these reactions, the Fe^{II} precursor (0.1 eq, 5 mM in MeCN) was stirred with ^{s}PhIO (1 eq) for either 1 or 10 min. Optically, the color changed to a purple color associated with the formation of the peroxido species. From UV−vis−NIR measurements, it is known that under these conditions after 1 min, the peroxide complex is completely formed (see the SI). After 1 or 10 min, the substrate (thioanisole, 5 eq) was added to the reaction mixture to start the catalytic transformation. For the workup, the vials were taken out of the glovebox after 1 or 6 h reaction time, and the solutions were filtered over a silica pipet column to separate the iron catalysts. The columns were washed with 3 mL of EtOAc, and the combined filtrate was evaporated at 40 °C. The sulfoxidation yields were determined by ^{1}H NMR spectroscopy. Therefore, 1,3,5-trimethoxybenzene (5 to 15 mg − exact amount noted) was added as the internal standard to the residue, which was dissolved CD_2Cl_2. All experiments were performed thrice. Yields are with respect to used amount of oxidant. See the Supporting Information for more details.

X-ray Crystal Structure Determinations. Crystal data and details of the structure determinations are compiled in Tables S1 and S2. Full shells of intensity data were collected at low temperature with a Bruker AXS Smart 1000 CCD diffractometer (Mo-K_a radiation, sealed X-ray tube, and graphite monochromator). Detector frames (w- and j-scans, scan width 0.4, and 0.5°) were integrated by profile fitting.[80−82] Data were corrected for air and detector absorption and Lorentz and polarization effects[83] and scaled essentially by application of appropriate spherical harmonic functions.[83,84] Absorption by the crystal was treated with a semiempirical multiscan method (as part of the scaling procedure) and augmented by a spherical correction.[84−86] The structures were solved by the charge flip procedure[87−89] and refined by full-matrix least-squares methods based on F^2 against all unique reflections.[90−93] All non-hydrogen atoms were given anisotropic displacement parameters. Hydrogen atoms were generally input at calculated positions and refined with a riding model.[91,94−96] In the structure of $L^1{*}OH_2$ most hydrogen atoms were located in a difference Fourier synthesis following an exponentially weighted high-angle refinement[97] and refined, except those of the methyl groups, which were treated as variable geometry rigid groups with local C_{3v} symmetry.[91,94−96] The refined positions of the hydrogen atoms of solvent water were close to those calculated to maximize hydrogen bonding,[97] employing atomic charges calculated from partial equalization of orbital electronegativity.[98,99] The hydrogen atoms of the coordinated water molecule in $[(L^1)Fe^{II}(OH_2)]^{2+}$ were located as weak peaks in a difference Fourier map and were fully refined. Disorder of one of the triflate anions was modeled by refinement of two rigid moieties with similarity restraints or constraints applied to the anisotropic displacement parameters.[94−96,100,101]

CCDC 2306135 and 2354017 contain the supplementary crystallographic data for this paper. These data can be obtained free of charge from the Cambridge Crystallographic Data Centre's and FIZ Karlsruhe's joint Access Service via https://www.ccdc.cam.ac.uk/structures/.

DFT Calculations. These were performed with Gaussian16[102−105] using B3LYP (hybrid GGA)[104] and B3LYP-D3 (hybrid GGA with dispersion correction terms) functionals for the optimization, along with the combination of LanL2DZ[106] for Fe and 6-31G* for the remaining atoms. For water model calculations, we optimized the geometries of intermediates, the reactant complex, and transition states with the B3LYP-D3 functional.[107] The methodology employed is grounded in prior research in this field. This approach is also validated by complementary findings from our group[108,109] and a benchmark study on the sulfoxidation of thioanisole by a nonheme Fe^{IV}=O catalyst, where it was shown that the B3LYP functional

https://doi.org/10.1021/acs.inorgchem.5c01373
Inorg. Chem. 2025, 64, 17672−17686

effectively reproduces experimental trends and absolute values of the free energy of activation.[67] Other studies have also shown B3LYP's effectiveness in predicting transition state geometries and molecular structures.[110,111] Our group also established B3LYP's efficiency in producing correct ground states for *ortho*-hydroxylation of aromatic substrates by nonheme Fe^{III}−OOH and Fe^{IV}=O complexes. Therefore, we selected B3LYP-D3 for this study due to its established accuracy in structural parameters, spin state energetics, and spectroscopic properties.[109] To assess and analyze the role of solvation in the spin state energetics, we have also performed optimization with solvation included and found that spin-state ordering is not altered here (see Table S7 in the Supporting Information).

To refine the energies of B3LYP-D3/LanL2TZ and 6-31G* optimized geometries, we conducted single-point energy calculations using a higher level basis set with the B3LYP-D3/TZVP (all atoms) set, which is the primarily used level of theory. The solvation energies were computed by using the PCM[112] and SMD solvation models.[113,114] Frequency calculations were performed on the optimized structures to confirm their status as minima on the potential energy surface (PES) and to calculate zero-point energy corrections. The fragment approach in Gaussian16 was utilized to facilitate smooth convergence, particularly in the case of the radical intermediates.

The ORCA 4.2 package[115] was employed for calculating the absorption spectra, Mössbauer, and EPR parameters. Time-dependent density functional theory (TDDFT), implemented in the ORCA, was utilized to calculate the excitation energies. To obtain electronic transitions via TDDFT calculations of various intermediates, the B3LYP functional and ZORA-def2-TZVP basis[116] set for all atoms[117] was used, and the RIJCOSX approximation with the def2/J auxiliary basis set was employed. *g* tensors were calculated using the B3LYP functional with the combination of the DKH-def2-TZVP basis set for Fe and the def2-SVP basis set for all other atoms. The Mössbauer data were obtained using the B3LYP functional along with the TZVP basis set. The isomer shift value was calculated with an established procedure.[118] We have also calculated the isomer shift using the CP(PPP) basis set, which yielded results similar to those obtained with the TZVP basis set, considering the standard deviation (regression law for B3LYP/TZVP (α = −0.298, β = 1.118, C = 11,580), for B3LYP/CP(PPP) (α = −0.366, β = 2.852, C = 11,810)). While both computed sets are similar, B3LYP/TZVP was found to yield a slightly better match to the experimental values.

■ ASSOCIATED CONTENT

Supporting Information

The Supporting Information is available free of charge at https://pubs.acs.org/doi/10.1021/acs.inorgchem.5c01373.

Experimental details, X-ray crystal structure analyses of the ligand and the iron(II) precursor, full details of the DFT based mechanistic analysis, additional UV−vis−NIR, EPR, Mössbauer, and ESI-MS data, kinetics plots, yields of the catalytic reactions and reference NMR data (PDF)

Accession Codes

Deposition Numbers 2306135 and 2354017 contain the supplementary crystallographic data for this paper. These data can be obtained free of charge via the joint Cambridge Crystallographic Data Centre (CCDC) and Fachinformationszentrum Karlsruhe Access Structures service.

■ AUTHOR INFORMATION

Corresponding Author

Peter Comba − *Anorganisch-Chemisches Institut, Universität Heidelberg, Heidelberg D-69120, Germany; Interdisziplinäres Zentrum für Wissenschaftliches Rechnen (IWR), Universität Heidelberg, Heidelberg D-69120, Germany;* orcid.org/0000-0001-7796-3532; Email: peter.comba@aci.uni-heidelberg.de

Authors

Katharina Bleher − *Anorganisch-Chemisches Institut, Universität Heidelberg, Heidelberg D-69120, Germany; Institute of Functional Interfaces, Karlsruhe Institute of Technology, Eggenstein-Leopoldshafen 76344, Germany;* orcid.org/0009-0002-0589-9601

Thakur Rochak Kumar Rana − *Department of Chemistry, Indian Institution of Technology Bombay, Mumbai, Maharashtra 400076, India*

Thomas Josephy − *Anorganisch-Chemisches Institut, Universität Heidelberg, Heidelberg D-69120, Germany*

Fridolin Röhs − *Lehrstuhl für Anorganische Chemie I, Fakultät für Chemie, Universität Bielefeld, Bielefeld D-33615, Germany*

Thorsten Glaser − *Lehrstuhl für Anorganische Chemie I, Fakultät für Chemie, Universität Bielefeld, Bielefeld D-33615, Germany*

Hubert Wadepohl − *Anorganisch-Chemisches Institut, Universität Heidelberg, Heidelberg D-69120, Germany*

Gopalan Rajaraman − *Department of Chemistry, Indian Institution of Technology Bombay, Mumbai, Maharashtra 400076, India;* orcid.org/0000-0001-6133-3026

Complete contact information is available at: https://pubs.acs.org/10.1021/acs.inorgchem.5c01373

Author Contributions

#K.B. and T.R.K.R. have equal contributions.

Notes

The authors declare no competing financial interest.

■ ACKNOWLEDGMENTS

Financial support by the University of Heidelberg is gratefully acknowledged, as is financial support by the German Science Foundation (DFG) within the Research Unit FOR 5215 "Bioinspired Oxidation Catalysis with Iron Complexes "BioOxCat") to P.C. (TP4) and T.G. (TP1). This study was conducted within the Max Planck School Matter to Life, supported by the BMBF in collaboration with the Max Planck Society. G.R. would like to acknowledge SERB for funding (CRG/2022/001697; SB/SJF/2019-20/12). T.R.K.R. acknowledges financial support from the Prime Minister's Research Fellowship (PMRF).

■ REFERENCES

(1) Yano, J.; Yachandra, V. Mn4Ca cluster in photosynthesis: where and how water is oxidized to dioxygen. *Chem. Rev.* **2014**, *114*, 4175−4205.

(2) Junge, W. Oxygenic photosynthesis: history, status and perspective. *Q. Rev. Biophys.* **2019**, *52*, No. e1.

(3) Vinyard, D. J.; Brudvig, G. W. Progress toward a molecular mechanism of water oxidation in photosystem II. *Annu. Rev. Phys. Chem.* **2017**, *68*, 101−116.

(4) Cammack, R.; Frey, M.; Robson, R. *Hydrogen as a Fuel: Learning from Nature*; Taylor & Francis, 2002.

(5) Rand, D. A. J.; Dell, R. M. *Hydrogen Energy: Challenges and Prospects* RSC Publishing, 2008.

(6) Fukuzumi, S.; Yamada, Y.; Karlin, K. D. Hydrogen peroxide as a sustainable energy carrier: electrocatalytic production of hydrogen peroxide and the fuel cell. *Electrochim. Acta* **2012**, *82*, 493−511.

(7) Sordakis, K.; Tang, C.; Vogt, L. K.; Junge, H.; Dyson, P. J.; Beller, M.; Laurenczy, G. Homogeneous catalysis for sustainable hydrogen storage in formic acid and alcohols. *Chem. Rev.* **2018**, *118*, 372−433.
(8) Olah, G. A. Towards oil independence through renewable methanol chemistry. *Angew. Chem., Int. Ed.* **2012**, *52*, 104−107.
(9) Bordet, A.; Leitner, W. Adaptive catalytic systems for chemical energy conversion. *Angew. Chem., Int. Ed.* **2023**, *62*, No. e202301956.
(10) Limburg, J.; Vrettos, J. S.; Laible-Sands, L. M.; Rheingold, A. L.; Crabtree, R. H.; Brudvig, G. W. A functional model for O-O bond formation by the O2 evolving complex in photosystem II. *Science* **1999**, *283*, 1524−1527.
(11) Fillol, J. L.; Codolà, Z.; Garcia-Bosch, I.; Gómez, L.; Pla, J. J.; Costas, M. Efficient water oxidation catalysts based on readily available iron coordination complexes. *Nat. Chem.* **2011**, *3*, 807−813.
(12) Kroll, N.; Speckmann, I.; Schoknecht, M.; Gülzow, J.; Diekmann, M.; Pfrommer, J.; Stritt, A.; Schlangen, M.; Grohmann, A.; Hörner, G. O-O bond formation and liberation of dioxygen mediated by N5-coordinate non-heme iron(IV)complexes. *Angew. Chem., Int. Ed.* **2019**, *58*, 13472−13478.
(13) Zhang, X.-P.; Chandra, A.; Lee, Y.-M.; Cao, R.; Ray, K.; Nam, W. Transition metal-mediated O-O bond formation and activation in chemistry and biology. *Chem. Soc. Rev.* **2021**, *50*, 4804−4811.
(14) Hong, Y. H.; Lee, Y.-M.; Fukuzumi, S.; Nam, W. Seeing the key intermediates in bioinspired nonheme iron complex-catalyzed water oxidation. *Chem.* **2024**, *10*, 1755−1765.
(15) Lionetti, D.; Suseno, S.; Shiau, A. A.; de Ruiter, G.; Agapie, T. Redox processes involving oxygen: the surprising influence of redox-inactive Lewis acids. *J. Am. Chem. Soc. Au* **2024**, *4*, 344−368.
(16) Najafpour, M. M.; Renger, G.; Holynska, M.; Moghaddam, A. N.; Aro, E.-M.; Carpentier, R.; Nishihara, H.; Eaton-Rye, J. J.; Shen, J.-R.; Allakhverdiev, S. I. Manganese compounds as water-oxidizing catalysts: from the natural water-oxidizing complex to nanosized manganese oxide structures. *Chem. Rev.* **2016**, *116*, 2886−2936.
(17) Price, J. C.; Barr, E. W.; Tirupati, B.; Bollinger, J. M., Jr.; Krebs, C. The First Direct Characterization of a High-Valent Iron Intermediate in the Reaction of an α-Ketoglutarate-Dependent Dioxygenase: A High-Spin Fe(IV) Complex in Taurine/α-Ketoglutarate Dioxygenase (TauD) from Escherichia coli. *Biochemistry* **2003**, *42*, 7497−7508.
(18) Krebs, C.; Galonici Fujimori, D.; Walsh, C. T.; Bollinger, J. M., Jr. Non-heme Fe (IV)−oxo intermediates. *Acc. Chem. Res.* **2007**, *40*, 484−492.
(19) Rohde, J.-U.; In, J.-H.; Lim, M. H.; Brennessel, W. W.; Bukowski, M. R.; Stubna, A.; Münck, E.; Nam, W.; Que, L., Jr. Crystallographic and Spectroscopic Characterization of a Nonheme Fe^{IV}=O Complex. *Science* **2003**, *299*, 1037−1039.
(20) Hohenberger, J.; Ray, K.; Meyer, K. The biology and chemistry of high-valent iron-oxo and iron-nitrido complexes. *Nat. Commun.* **2012**, *3* (1), 720.
(21) Bukowski, M. R.; Comba, P.; Limberg, C.; Merz, M.; Que, L., Jr.; Wistuba, T. Bispidine ligand effects on iron/hydrogen peroxide chemistry. *Angew. Chem., Int. Ed.* **2004**, *43* (10), 1283−1287.
(22) Comba, P.; Kerscher, M.; Schiek, W. Bispidine coordination chemistry. *Prog. Inorg. Chem.* **2007**, *55*, 613−704.
(23) Comba, P.; Kerscher, M.; Krause, M.; Schöler, H. F. Iron-catalysed oxidation and halogenation of organic matter in nature. *Env. Chem.* **2015**, *12*, 381−395.
(24) Comba, P.; Kerscher, M.; Rück, K.; Starke, M. Bispidines for radiopharmaceuticals. *Dalton Trans.* **2018**, *47*, 9202−9220.
(25) Comba, P.; Kerscher, M.; Merz, M.; Müller, V.; Pritzkow, H.; Remenyi, R.; Schiek, W.; Xiong, Y. Structural variation in transition metal bispidine complexes. *Chem.—Eur. J.* **2002**, *8*, 5750−5760.
(26) Comba, P.; Schiek, W. Fit and misfit between ligands and metal ions. *Coord. Chem. Rev.* **2003**, *238*−*239*, 21−29.
(27) Bleiholder, C.; Börzel, H.; Comba, P.; Ferrari, R.; Heydt, A.; Kerscher, M.; Kuwata, S.; Laurenczy, G.; Lawrance, G. A.; Lienke, A.; Martin, B.; Merz, M.; Nuber, B.; Pritzkow, H. Coordination chemistry of a new rigid, hexadentate bispidine-based bis(amine)tetrakis-(pyridine) ligand. *Inorg. Chem.* **2005**, *44* (22), 8145−8155.
(28) Bleher, K.; Cieslik, P.; Comba, P. Bispidine coordination chemistry. *Dalton Trans. (Perspective)* **2025**, *54*, 4405−4431.
(29) Comba, P.; Fukuzumi, S.; Kotani, H.; Wunderlich, S. Electron transfer properties of an efficient nonheme iron oxidation catalyst with a tetradentate bispidine ligand. *Angew. Chem., Int. Ed.* **2010**, *49*, 2622−2625.
(30) Wang, D.; Ray, K.; Collins, M. J.; Farquhar, E. R.; Frisch, J. R.; Gomez, L.; Jackson, T. A.; Kerscher, M.; Waleska, A.; Comba, P.; Costas, M.; Que, L., Jr. Non-heme oxoiron(IV) complexes of pentadentate N5 ligands: spectroscopy, electrochemistry and oxidative reactivity. *Chem. Sci.* **2013**, *4*, 282−291.
(31) Comba, P.; Nunn, G.; Scherz, F.; Walton, P. H. Intermediate-spin iron(IV)-oxido species with record reactivity. *Faraday Discuss.* **2022**, *234*, 232−244.
(32) Abu-Odeh, M.; Bleher, K.; Britto, N. J.; Comba, P.; Gast, M.; Jaccob, M.; Kerscher, M.; Krieg, S.; Kurth, M. Pathways of the extremely reactive iron(IV)oxido complexes with tetradentate bispidine ligands. *Chem.—Eur. J.* **2021**, *27*, 11377−11390.
(33) Bleher, K.; Comba, P.; Faltermeier, D.; Gupta, A.; Kerscher, M.; Krieg, S.; Martin, B.; Velmurugan, G.; Yang, S. Non-heme-iron-catalyzed halogenation of unactivated carbon-hydrogen bonds. *Chem.—Eur. J.* **2022**, *28*, No. e202103452.
(34) Comba, P.; Maurer, M.; Vadivelu, P. Oxidation of cyclohexane by a high-valent iron bispidine complex − a combined experimental and computational mechanistic study. *J. Phys. Chem. (A)* **2008**, *112*, 13028−13036.
(35) Comba, P.; Maurer, M.; Vadivelu, P. Oxidation of cyclohexane by high-valent bispidine complexes: tetradentate vs. pentadentate ligands. *Inorg. Chem.* **2009**, *48*, 10389−10396.
(36) Cook, S. A.; Borovik, A. S. Molecular designs for controlling the local environments around metal ions. *Acc. Chem. Res.* **2015**, *48* (8), 2407−2414.
(37) Würtele, C.; Gaoutchenova, E.; Harms, K.; Holthausen, M. C.; Sundermeyer, J.; Schindler, S. Crystallographic characterization of a synthetic 1:1 end-on copper dioxygen adduct complex. *Angew. Chem.* **2006**, *118*, 3951.
(38) Bosch, S.; Comba, P.; Gahan, L. R.; Schenk, G. 'Dinuclear zinc(II) complexes with hydrogen bond donors as structural and functional phosphatase models. *Inorg. Chem.* **2014**, *53*, 9036−9051.
(39) Battistella, B.; Warm, K.; Cula, B.; Lu, B.; Hildebrandt, P.; Kuhlmann, U.; Dau, H.; Mebs, S.; Ray, K. J. The influence of secondary interactions on the [Ni(O2)]+ mediated aldehyde oxidation reactions. *Inorg. Biochem.* **2022**, *227*, No. 111668.
(40) Cheaib, K.; Mubarak, M. Q. E.; Sénécahl-David, K.; Herrero, C.; Guillot, R.; Clémancey, M.; Latour, J.-M.; de Visser, S. P.; Mahy, J.-P.; Banse, F.; Avenier, F. Selective formation of an FeIVO or an FeIIIOOH intermediate from Fe(II) and H2O2: controlled heterolytic versus homolytic oxygen-oxygen bond cleavage by the second coordination sphere. *Angew. Chem., Int. Ed.* **2019**, *58*, 854−858.
(41) Yadav, S.; Lyons, R. S.; Readi-Brown, Z.; Siegler, M. A.; Goldberg, D. P. Influence of the second coordination sphere on O2 activation by a nonheme iron(II) thiolate complex. *J. Inorg. Biochem.* **2025**, *264*, No. 112776.
(42) Bleher, K.; Comba, P.; Kass, D.; Ray, K.; Wadepohl, H. Reactivities of iron(IV)-oxido compounds with pentadentate bispidine ligands. *J. Inorg. Biochem.* **2023**, *241*, No. 112123.
(43) Bautz, J.; Bukowski, M.; Kerscher, M.; Stubna, A.; Comba, P.; Lienke, A.; Münck, E.; Que, L., Jr Aqueous Oxoiron(IV) Formation at pH 2−6 from a nonheme Iron(II) Complex and H_2O_2. *Angew. Chem., Int. Ed.* **2006**, *45*, 5681.
(44) Bautz, J.; Comba, P.; Que, L., Jr. Spin-crossover in an iron(III)-bipidine-alkylperoxide system. *Inorg. Chem.* **2006**, *45*, 7077.
(45) Bukowski, M. R.; Comba, P.; Lienke, A.; Limberg, C.; Lopez de Laorden, C.; Mas-Balleste, R.; Merz, M.; Que, L., Jr. Catalytic oxidation of olefins in bispidine iron (II)/H_2O_2 systems. *Angew. Chem., Int. Ed.* **2006**, *45*, 3446.

https://doi.org/10.1021/acs.inorgchem.5c01373
Inorg. Chem. 2025, 64, 17672−17686

(46) Bautz, J.; Comba, P.; Lopez de Laorden, C.; Menzel, M.; Rajaraman, G. Biomimetic high-valent nonheme iron(IV) oxidants for the cis-dihydroxylation and epoxidation of olefins. *Angew. Chem., Int. Ed.* **2007**, *46*, 8067−8070.
(47) Comba, P.; Faltermeier, D.; Krieg, S.; Martin, B.; Rajaraman, G. Spin state of iron(IV)oxido complexes with tetradentate bispidin ligands. *Dalton Trans.* **2020**, *49*, 2888−2894.
(48) Krieg, S. Heidelberg University: Heidelberg 2019.
(49) Kovaleva, E. G.; Lipscomb, J. D. Versatility of biological non-heme Fe(II) centers in oxygen activation reactions. *Nat. Chem. Biol.* **2008**, *4*, 186−193.
(50) McQuilken, A. C.; Jiang, Y.; Siegler, M. A.; Goldberg, D. P. Addition of dioxygen to an N4S(thiolate) iron(II) cysteine dioxygenase model gives a structurally characterized sulfinato-iron(II) complex. *J. Am. Chem. Soc.* **2012**, *134*, 8758−8761.
(51) Hong, S.; Sutherlin, K. D.; Park, J.; Kwon, E.; Siegler, M. A.; Solomon, E. I.; Nam, W. Crystallographic and spectroscopic characterization and reactivities of a mononuclear non-haem iron-(III)-superoxo complex. *Nature Comm.* **2014**, *5*, 5440.
(52) Chiang, C.-W.; Kleespies, S. T.; Stout, H. D.; Meier, K. K.; Li, P.-Y.; Boominaar, E. L.; Que, L., Jr.; Münck, E.; Lee, W.-Z. Characterization of a Paramagnetic Mononuclear Nonheme Iron-Superoxo Complex. *J. Am. Chem. Soc.* **2014**, *136*, 10846−10849.
(53) Blakely, M. N.; Dedushko, M. A.; Yan Poon, P. C.; Villar-Acevedo, G.; Kovacs, J. A. Formation of a Reactive, Alkyl Thiolate-Ligated FeIII-Superoxo Intermediate Derived from Dioxygen. *J. Am. Chem. Soc.* **2019**, *141* (5), 1867−1870.
(54) Winslow, C.; Lee, H. B.; Field, M. J.; Teat, S. J.; Rittle, J. Structure and reactivity of a high-spin, nonheme iron(III)-superoxo complex supported by phophinimide ligands. *J. Am. Chem. Soc.* **2021**, *143* (34), 13686−13693.
(55) Mukherjee, G.; Velmurugan, G.; Kerscher, M.; Satpathy, J. K.; Sastri, C. V.; Comba, P. Mechanistic insights into amphoteric reactivity of an iron-bispidine complex. *Chem.—Eur. J.* **2023**, *30*, No. e202303127.
(56) Bleher, K.; Comba, P.; Gross, J.; Josephy, T. ESI and tandem MS for mechanistic studies of high-valent metal complexes. *Dalton Trans. (Perspective)* **2022**, *51*, 8625−8639.
(57) England, J.; Guo, Y.; Farquhar, E. R.; Young, V. G., Jr.; Münck, E.; Que, L., Jr The Crystal Structure of a High-Spin Oxoiron(IV) Complex and Characterization of Its Self-Decay Pathway. *J. Am. Chem. Soc.* **2010**, *132*, 8635−8644.
(58) Comba, P.; Wunderlich, S. Iron-catalyzed halogenation of alkanes: modeling of nonheme halogenases by experiment and DFT. *Chem.—Eur. J.* **2010**, *16* (24), 7293−7299.
(59) Hädeler, J.; Velmurugan, G.; Lauer, R.; Radhamani, R.; Keppler, F.; Comba, P. Natural abiotic iron-oxido-mediated formation of C1 and C2 compounds from environmentally important methyl-substituted substrates. *J. Am. Chem. Soc.* **2023**, *145*, 24590−24602.
(60) CCl_3Br or CH_2Br_2 are known to efficiently trap alkyl radicals to produce the corresponding brominated products, which are stable under the MS conditions used.[47,50,51]
(61) Karimadom, B. R.; Meyerstein, D.; Kornweitz, H. On the nature of FeIV = Oaq in aqueous media: a DFT analysis. *ChemPhysChem* **2023**, *24*, No. e202300508.
(62) Chen, J.; Sardjan, A. S.; de Roo, C. M.; Di Berto Mancini, M.; Draksharapu, A.; Angelone, D.; Hage, R.; Swart, M.; Browne, W. R. Generation of [(N4py)Fe(IV)═O]2+ through heterolytic O-O bond cleavage in [(N4py)Fe(II)(OOH)]+. *Inorg. Chem.* **2025**, *64*, 9408−9417.
(63) Phapale, D.; Sharma, V.; Saini, A.; Sharma, S.; Kumar, P.; Kumar, R.; Shanmugam, M.; Draksharapu, A.; Dutta, A.; McInnes, E. J. L.; Collison, D.; Rajaraman, G.; Shanmugam, M. Capturing the elusive [RuV = O]+ intermediate in water oxidation. *ACS Catal.* **2024**, *14*, 11893−11904.
(64) de Gracia Triviño, J. A.; Ahlquist, M. S. G. Removing the barrier in O-O bond formation via the combination of intramolecular radical coupling and the oxide relay mechanism. *J. Phys. Chem. A* **2024**, *128*, 3794−3800.
(65) Kumar, R.; Ansari, A.; Comba, P.; Rajaraman, G. Rebound or cage escape? The role of the rebound barrier for the reactivity o non-heme high-valent Fe^{IV}=O species. *Chem.—Eur. J.* **2023**, *30*, No. e202303300.
(66) Costas, M.; Mehn, M. P.; Jensen, M. P.; Que, L., Jr. *Chem. Rev.* **2004**, *104*, 939.
(67) Reinhard, F. G. C.; Faponle, A. S.; de Visser, S. P. *J. Phys. Chem. A* **2016**, *120*, 9805−9814.
(68) Jaccob, M.; Comba, P.; Maurer, M.; Vadivelu, P.; Venuvanalingam, P. A combined experimental and computational study on the sulfoxidation by high-valent iron bispidine complexes. *Dalton Trans.* **2011**, *40*, 11276−11281.
(69) Harvey, J. Understanding the kinetics of spin-forbidden chemical reactions. *Phys. Chem. Chem. Phys.* **2007**, *9*, 331−349.
(70) Cho, J.; Jeon, S.; Wilson, S. A.; Liu, L. V.; Kang, E. A.; Braymer, J. J.; Lim, M. H.; Hedman, B.; Hodgson, K. O.; Valentine, J. S.; Solomon, E. I.; Nam, W. Structure and reactivity of a mononuclear non-haem iron(III)-peroxo complexes. *Nature* **2011**, *478*, 502−505.
(71) Zhu, W.; Wu, P.; Larson, V. A.; Kumar, A.; Li, X.-X.; Seo, M. S.; Lee, Y.-M.; Wang, B.; Lehnert, N.; Nam, W. Electronic structure and reactivity of mononuclear nonheme iro-peroxo complexes as biomimetic model of Rieske oxygenases: ring size effects of macrocyclic ligands. *J. Am. Chem. Soc.* **2024**, *146*, 250−262.
(72) Kim, Y. M.; Cho, K.-B.; Cho, J.; Wang, B.; Li, C.; Shaik, S.; Nam, W. A mononuclear non-heme high-spin iron(III)-hydroperoxo complex as an active oxidant in sulfoxidation reactions. *J. Am. Chem. Soc.* **2013**, *135*, 8838−8841.
(73) Thibon, A.; Bartoli, J.-F.; Bourcier, S.; Banse, F. Mononuclear iron complexes relevant to nonheme iron oxygenases. Synthesis, characterizations and reactivity of Fe-oxo and Fe-peroxo intermediates. *Dalton Trans.* **2009**, 9587−9594.
(74) Faponle, A. S.; Quesne, M. G.; Sastri, C. V.; Banse, F.; de Visser, S. P. Differences and comparisons of the properties and reactivities of iron(III)-hydroperoxo complexes with saturated coordination sphere. *Chem.—Eur. J.* **2015**, *21*, 1221−1236.
(75) Comba, P.; Rajaraman, G. Epoxidation and 1,2-dihydroxylation of alkenes by a nonheme iron model system - DFT supports the mechanism proposed by experiment. *Inorg. Chem.* **2008**, *47*, 78−93.
(76) Comba, P.; Fukuzumi, S.; Koke, C.; Martin, B.; Löhr, A.; Straub, J. A bispidine iron(IV) oxo complex in the entatic state. *Angew. Chem., Int. Ed.* **2016**, *55*, 11129−11133.
(77) Peters, A.; Kaifer, E.; Himmel, H. J. 1,2,4,5-tetrakis-(tetramethylguanidino)benzene: synthesis and properties of a new molecular electron donor. *Eur. J. Org. Chem.* **2008**, *2008*, 5907−5914.
(78) Macikenas, D.; Skrzypczak-Jankun, E.; Protasiewicz, J. D. A new class of iodonium ylides engineered as soluble primary oxo and nitrene sources. *J. Am. Chem. Soc.* **1999**, *121*, 7164−7165.
(79) Börzel, H.; Comba, P.; Hagen, K. S.; Merz, M.; Lampeka, Y. D.; Lienke, A.; Linti, G.; Pritzkow, H.; Tsymbal, L. V. Iron coordination chemistry with tetra-, penta- and hexadentate bispidine-type ligands. *Inorg. Chim. Acta* **2002**, *337*, 407−419.
(80) Blessing, R. H. Data reduction and error analysis for accurate single crystal diffraction intensities. *Cryst. Rev.* **1987**, *1*, 3−58.
(81) Kabsch, K. *International Tables for Crystallography*, Rossmann, M. G.; Arnold, E. Ed.; Vol. F, Ch.11.3; Kluwer Academic Publishers, 2001.
(82) *SMART*; Bruker AXS GmbH: Karlsruhe, Germany, 2003. (accessed.
(83) *SAINT*; Bruker AXS GmbH: Karlsruhe, Germany, 1997−2019. (accessed.
(84) Blessing, R. H. An empirical correction for absorption anisotropy. *Acta Crystallogr.* **1995**, *A51*, 33−38.
(85) *SADABS*; SADABS, Bruker AXS: Karlsruhe, 2004−2016. (accessed.
(86) Krause, L.; Herbst-Irmer, R.; Sheldrick, G. M.; Stalke, D. Comparison of silver and molybdenum microfocus X-ray sources for single-crystal structure determination. *J. Appl. Crystallogr.* **2015**, *48*, 3−10.

https://doi.org/10.1021/acs.inorgchem.5c01373
Inorg. Chem. 2025, 64, 17672−17686

(87) *SUPERFLIP*; EPF Lausanne, Switzerland and Fyzikalni ustav AV CR: Prague, Czech Republic, 2007−2014. (accessed.
(88) Palatinus, L.; Chapuis, G. SUPERFLIP - a computer program for the solution of crystal structures by charge flipping in arbitrary dimensions. *J. Appl. Crystallogr.* **2007**, *40*, 786−790.
(89) Palatinus, L. The charge-flipping algorithm in crystallography. *Acta Crystallogr.* **2013**, *B69*, 1−16.
(90) *SHELXL-20xx*; University of Göttingen and Bruker AXS GmbH: Karlsruhe, Germany, 2012−2018. (accessed.
(91) Robinson, W.; Sheldrick, G. M. In *Crystallographic Computing 4*, Isaacs, M.; Taylor, M. R. Eds.; Ch.22, IUCr and Oxford University Press, 1988.
(92) Sheldrick, G. M. A short history of SHELX. *Acta Crystallogr.* **2008**, *A64*, 112−122.
(93) Sheldrick, G. M. Crystal structure refinement with SHELXL. *Acta Crystallogr.* **2015**, *A71*, 3−8.
(94) Watkin, D. In *Crystallographics Computing 4*, Isaaks, N. W.; Taylor, M. R. Eds.; Ch. 8, IUCr and Oxford University Press, 1988.
(95) Müller, P.; Herbst-Irmer, R.; Spek, A. L.; Schneider, T. R.; Sawaya, M. R. In *Crystal Structure Refinement*, Müller, P. Ed.; Vol. Ch. 5; Oxford University Press, 2006.
(96) Watkin, D. Structure refinement: some background theory and practical strategies. *J. Appl. Crystallogr.* **2008**, *41*, 491−522.
(97) Dunitz, J. D.; Seiler, P. Least-squares refinement and weighted difference synthesis. *Acta Crystallogr.* **1973**, *B29*, 589−595.
(98) Nardelli, M. Modeling hydroxyl and water H atoms. *J. Appl. Crystallogr.* **1999**, *32*, 563−571.
(99) Nardelli, M. A calculator program for calculating hydrogen atom coordinates. Computers and Chemistry. *J. Appl. Crystallogr.* **1982**, *6*, 139−152.
(100) Rollett, J. S. In *Crystallographic Computing*, Ahmed, F. R.; Hall, S. R.; Huber, C. P. Eds.; Munksgaard, International Booksellers and Publishers 1970; p 167.
(101) Thorn, A.; Dittrich, B.; Sheldrick, G. M. Enhanced rigid-bond restraints. *Acta Crystallogr.* **2012**, *A68*, 448−451.
(102) Frisch, M. *Gaussian 09*, Revision D.01; Gaussian, Inc.: Wallingford CT, 2009. (accessed.
(103) Lee, C.; Yang, W.; Parr, R. G. Development of the Colle-Salvetti correlation-energy formula into a functional of the electron-density. *Phys. Rev. B* **1988**, *37* (2), 785−789.
(104) Andersson, M. P.; Uvdal, P. New scale factors for harmonic vibrational frequencies using the B3LYP density functional method with the triple-zeta basis set 6−311+G(d,p). *J. Phys. Chem. A* **2005**, *109*, 2937−2941.
(105) Stephens, P. J.; Delvin, F. J.; Chabalowski, C. F.; Frisch, M. J. Ab-initio calculation of vibrational absorption and circular-dichroism spectra using density-functional force-fields. *J. Phys. Chem.* **1994**, *98*, 11623−11627.
(106) Hay, P. J.; Wadt, W. R. Ab-initio effective core potentials for molecular calculations - potentials for the transition-metal atoms Sc to Hg. *J. Chem. Phys.* **1985**, *82*, 270−283.
(107) Peintinger, M. F.; Oliveira, D. V.; Bredow, T. Consistent gaussian basis sets of triple-zeta valence with polarization quality for solid-state calculations. *J. Comput. Chem.* **2013**, *34*, 451−459.
(108) Sen, A.; Vyas, N.; Pandey, B.; Rajaraman, G. Deciphering the mechanism of oxygen transfer by non-heme Mn(IV)-oxo species: an ab initio and DFT exploration. *Dalton Trans.* **2020**, *49*, 10380−10393.
(109) Ansari, A.; Kaushik, A.; Rajaraman, G. Mechanistic insights on the ortho-hydroxylation of aromatic compounds by non-heme iron complex: a computational case study on the comparative oxidative ability of ferric-hydroperoxo and high-valent Fe(IV)═O and Fe(V)═O intermediates. *J. Am. Chem. Soc.* **2013**, *135*, 4235−4249.
(110) Chen, H.; Lai, W.; Shaik, S. Exchange-enhanced H-abstaction reactivity of high-valent nonheme iron(IV)-oxo from coupled cluster and density functional theories. *J. Phys. Chem. Lett.* **2010**, *1*, 1533−1540.
(111) Lundberg, M.; Siegbahn, P. E. M. Agreement between experiment and hybrid DFT calculations for O-H bond dissociation enthalpies in manganese complexes. *J. Comput. Chem.* **2005**, *26*, 661−667.
(112) Tomasi, J.; Mennucci, B.; Cammi, R. Quantum Mechanical Continuum Solvation Models. *Chem. Rev.* **2005**, *105*, 2999−3093.
(113) Andrae, D.; Haeussermann, U.; Dolg, M.; Stoll, H.; Preuss, H. Energy-adjusted abinitio pseudopotentials for the 2nd and 3rd row transition-elements. *Theoretica. Chimica. Acta* **1990**, *77*, 123−141.
(114) Cossi, M.; Rega, N.; Scalmani, G.; Barone, B. Energies, structures, and electronic properties of molecules in solution with the C-PCM solvation model. *J. Comput. Chem.* **2003**, *24* (6), 669−681.
(115) Neese, F. The ORCA program system. *Wiley Interdiscip. Rev. Comput. Mol. Sci.* **2012**, *2* (1), 73−78.
(116) Ahlrichs, R.; Weigend, F. Balanced basis sets of split valence, triple zeta valence and quadruple zeta valence quality for H to Rn: design and assessment of accuracy. *Phys. Chem.* **2005**, *7*, 3297−3305.
(117) Weigend, F. Hartree-Fock exchange fitting basis sets for H to Rn. *J. Comput. Chem.* **2008**, *29*, 167−175.
(118) Römelt, M.; Ye, S.; Neese, F. Calibration of modern density functional theory methods for the prediction of 57-Fe Mossbauer isomer shifts: meta-GGA and double-hybrid functionals. *Inorg. Chem.* **2009**, *48*, 784−785.

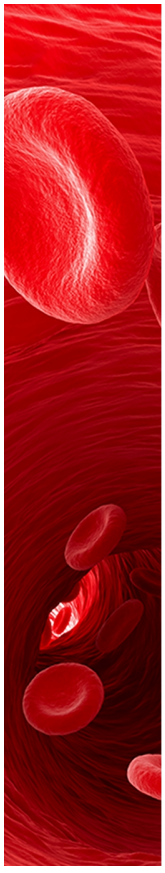
CAS BIOFINDER DISCOVERY PLATFORM™
CAS BIOFINDER HELPS YOU FIND YOUR NEXT BREAKTHROUGH FASTER
Navigate pathways, targets, and diseases with precision
Explore CAS BioFinder
CAS
A division of the American Chemical Society

https://doi.org/10.1021/acs.inorgchem.5c01373
Inorg. Chem. 2025, 64, 17672−17686